

Radical chemistry in the Pearl River Delta: observations and modeling of OH and HO₂ radicals in Shenzhen 2018

Xinping Yang^{1,2}, Keding Lu^{1,2,*}, Xuefei Ma^{1,2}, Yue Gao^{1,2}, Zhaofeng Tan³, Haichao Wang⁴, Xiaorui Chen^{1,2}, Xin Li^{1,2}, Xiaofeng Huang⁵, Lingyan He⁵, Mengxue Tang⁵, Bo Zhu⁵, Shiyi Chen^{1,2}, Huabin Dong^{1,2}, Limin Zeng^{1,2}, Yuanhang Zhang^{1,2,*}

¹State Key Joint Laboratory of Environmental Simulation and Pollution Control, College of Environmental Sciences and Engineering, Peking University, Beijing, China

²State Environmental Protection Key Laboratory of Atmospheric Ozone Pollution Control, Peking University, Beijing, China

³Institute of Energy and Climate Research, IEK-8: Troposphere, Forschungszentrum Juelich GmbH, Juelich, Germany

⁴School of Atmospheric Sciences, Sun Yat-Sen University, Zhuhai, China

⁵Laboratory of Atmospheric Observation Supersite, School of Environment and Energy, Peking University Shenzhen Graduate School, Shenzhen, China

Correspondence to: Keding Lu (k.lu@pku.edu.cn), Yuanhang Zhang (yhzhang@pku.edu.cn)

Abstract. The ambient radical concentrations were measured continuously by laser-induced fluorescence during the STORM (STudy of the Ozone foRmation Mechanism) campaign at the Shenzhen site, located in the Pearl River Delta in China, in the autumn of 2018. The diurnal maxima were $4.5 \times 10^6 \text{ cm}^{-3}$ for OH and $4.2 \times 10^8 \text{ cm}^{-3}$ for HO₂ (including an estimated interference of 23%-28% from RO₂ radicals during the daytime), respectively. The state-of-the-art chemical mechanism underestimated the observed OH concentration, similar to the other warm-season campaigns in China. The OH underestimation was attributable to the missing OH sources, which can be explained by the X mechanism. Good agreement between the observed and modeled OH concentrations was achieved when an additional numerical X equivalent to 0.1 ppb NO concentrations was added into the base model. The isomerization mechanism of RO₂ derived from isoprene contributed approximately 7% to the missing OH production rate and the oxidation of isoprene oxidation products (MACR and MVK) had no significant impact on the missing OH sources, demonstrating further exploration of unknown OH sources is necessary. A significant HO₂ heterogeneous uptake was found in this study, with an effective uptake coefficient of 0.3. **The model with the HO₂ heterogeneous uptake can simultaneously reproduce the OH and HO₂ concentrations when the amount of X changed from 0.1 to 0.25 ppb.** The ROx primary production rate was dominated by photolysis reactions, in which the HONO, O₃, HCHO, and carbonyls photolysis accounted for 29%, 16%, 16%, and 11% during the daytime, respectively. The ROx termination rate was dominated by the reaction of OH + NO₂ in the morning, and thereafter the radical self-combination gradually became the major sink of ROx in the afternoon. As the sum of the respective oxidation rates of the pollutants via reactions with oxidants, the atmospheric oxidation capacity was evaluated, with a peak of 11.8 ppb h⁻¹ around noontime. The ratio of $P(\text{O}_3)_{\text{net}}$ to AOC_{VOCs} , which indicates the yield of net ozone production from VOCs oxidation, trended to increase and then decrease as the NO concentration increased. The median ratios ranged within 1.0-4.5, with the maximum existing when the NO concentration was

带格式的: 下标

带格式的: 非上标/ 下标

带格式的: 下标

34 approximately 1 ppb. The nonlinear relationship between the yield of net ozone production from VOCs oxidation and NO
35 concentrations demonstrated that optimizing the NOx and VOCs control strategies is critical to controlling the ozone pollution
36 effectively in the future.

37 **1 Introduction**

38 Severe ambient ozone (O₃) pollution is one of China's most significant environmental challenges (Shu et al., 2020; Li et al.,
39 2019; Wang et al., 2020; Ma et al., 2019b; Wang et al., 2017a). Despite the reduction in emissions of O₃ precursors, O₃
40 concentration is increasing, especially in urban cities. The O₃ average trends for the focus megacity clusters are 3.1 ppb a⁻¹,
41 2.3 ppb a⁻¹, 0.56 ppb a⁻¹, and 1.6 ppb a⁻¹ for North China Plain (NCP), Yangtze River Delta (YRD), Pearl River Delta (PRD),
42 and Szechwan Basin (SCB), respectively (Li et al., 2019). The nonlinearity between O₃ and precursors illustrates that it is
43 necessary to explore the cause of O₃ production. The tropospheric O₃ is only generated in the photolysis of nitrogen dioxide
44 (NO₂) which is produced as the by-product within the radical cycling. Thus, the investigation of radical chemistry is critical to
45 controlling secondary pollution.

46 Hydroxyl radicals (OH), the dominant oxidant, control the atmospheric oxidation capacity (AOC) in the troposphere. The
47 OH radicals convert primary pollutants to secondary pollutants and are simultaneously transformed into peroxy radicals (HO₂
48 and RO₂). Within the interconvert of ROx (= OH, HO₂, and RO₂), secondary pollutants are generated, and thus the further
49 exploration of radical chemistry is significant. The radical closure experiment, an effective indicator for testing our
50 understanding of radical chemistry, has been conducted since the central role of OH radicals was recognized in the 1970s (Levy,
51 1971; Hofzumahaus et al., 2009). The underestimation of OH radicals in environments characterized by low nitrogen oxides
52 (NO) and high volatile organic compounds (VOCs) has been identified (Lu et al., 2013; Lu et al., 2012; Tan et al., 2017; Tan et
53 al., 2019; Yang et al., 2021; Hofzumahaus et al., 2009; Lelieveld et al., 2008; Whalley et al., 2011). New radical mechanisms
54 involving unclassical OH regeneration have been proposed, mainly including Leuven Isoprene Mechanism (LIM) and X
55 mechanism (Peeters and Muller, 2010; Peeters et al., 2014; Peeters et al., 2009; Hofzumahaus et al., 2009). The LIM which has
56 been integrated into the current radical mechanism is still insufficient to explain the OH missing sources. The X mechanism
57 was identified several times, but the amount of the numerical species, X, varied in different environments, and the nature of X
58 is still unknown (Hofzumahaus et al., 2009; Lu et al., 2013; Lu et al., 2012; Tan et al., 2017; Tan et al., 2019; Yang et al., 2021; Ma
59 et al., 2022a). Therefore, further exploration of radical regeneration sources is necessary.

60 Due to the strong photochemistry influenced by high temperatures and strong radiation, high-severe O₃ pollution appeared
61 to occur in YRD and PRD, especially in PRD (Ma et al., 2019b; Wang et al., 2017a). Radicals, the dominant oxidant in the
62 troposphere, have been measured during warm seasons in NCP (Yufa 2006, Wangdu 2014, and Beijing 2016), YRD (Taizhou
63 2018), SCB (Chengdu 2019), and PRD (Backgarden 2006, and Heshan 2014) in China (Lu et al., 2013; Lu et al., 2012; Tan et

al., 2017; Tan et al., 2019; Yang et al., 2021; Tan et al., 2021; Ma et al., 2022a). The radical observations in PRD, where the cities are suffering from severe O₃ pollution, have not been conducted since 2014, and thus the oxidation capacity here has not been clear in recent years. Therefore, we carried out a continuous comprehensive field campaign (STudy of the Ozone foRmation Mechanism - STORM) involving radical observations in Shenzhen, one of the megacities in PRD, in the autumn of 2018. Overall, the following will be reported in this study.

- (1) The observed radical concentrations, and the comparison between the radical observations and simulations.
- (2) The exploration of the unclassical OH regeneration sources based on the experimental budget.
- (3) The sources and sinks of ROx radicals.
- (4) The evaluation of the atmospheric oxidation capacity.

2 Methodology

2.1 Measurement site and instrumentation

The STORM campaign was conducted from September to October 2018 in Peking University Shenzhen Graduate School (22.60 deg N, 113.97 deg E), in the west of Shenzhen, Guangdong province. As shown in Fig. 1, this site, which belongs to the urban site, is located in the university town, and is surrounded by residential and commercial areas. The northwest of the site is close to the Shenzhen Wildlife Park, and the northeast is close to the Xili Golf Club (Yu et al., 2020). The Tanglang Mountain Park with active biogenic emissions is located about 1 km southeast of the site. Overall, this site has no significant local pollution sources nearby, but can represent the urban pollution characteristics (Huang et al., 2012a; Huang et al., 2012b; Gao et al., 2018).



Figure 1: Geographical location and surrounding environmental conditions of the measurement site in the STORM campaign (The maps are from <https://map.baidu.com>).

Most instruments were set up on the top of a four-story academic building (about 20 m). Besides HOx radicals measured by the Peking University-Laser Induced Fluorescence system (PKU-LIF) (see the details in Sect. 2.2), a comprehensive set of

87 trace gases was conducted to support the exploration of ~~the~~ radical chemistry, including meteorological parameters
88 (temperature, pressure, relative humidity, *etc.*), photolysis frequency, OH reactivity (k_{OH}) and the trace gases (NO, NO₂, O₃,
89 VOCs, *etc.*). k_{OH} was measured by the Laser flash Photolysis-Laser Induced Fluorescence ~~system~~ (LP-LIF)-~~system~~. Most of
90 the inorganic trace gases (O₃, CO, NO, NO₂, and SO₂) were simultaneously measured by two sets of instruments, and good
91 agreement was achieved within the uncertainty. VOCs species (alkanes, alkenes, aromatics, isoprene, and oxygenated VOCs
92 (OVOCs)) were measured using a gas chromatograph following a mass spectrometer (GC-MS). In addition, HONO and HCHO
93 were measured as well. Table S1 in the Supplementary Information presents the experimental details of the meteorological and
94 chemical parameters during this campaign.

95 2.2 The OH and HO₂ measurements

96 The OH and HO₂ radicals were measured by PKU-LIF based on the fluorescence assay by gas expansion (FAGE) technique.
97 The principle has been reported in previous studies, [and](#) only a brief description of the instrument is presented here. Further
98 detailed information on the instrument can be found in previous studies (Heard and Pilling, 2003; Fuchs et al., 2008; Holland
99 et al., 1995; Hofzumahaus et al., 1996; Fuchs et al., 2011).

100 In principle, OH resonance fluorescence is released in the OH excitation by a 308 nm pulsed laser, and then OH radicals are
101 detected directly. HO₂ radicals are converted into OH via NO, and then they are detected. The system contains a laser module
102 and a detection module. Ambient air was drawn into two independent, parallel, low-pressure (3.5 mBar) cells through two
103 parallel nozzles with 0.4 mm diameter pinhole. The OH radicals are excited into resonance fluorescence in the OH detection
104 cell and detected by micro-channel plate detectors (MCP). In the HO₂ detection cell, NO is injected and converts HO₂ to OH
105 radicals, and then OH radicals are excited by the laser and release resonance fluorescence. Besides, an OH reference cell in
106 which a large OH concentration is generated by pyrolysis of water vapor on a hot filament is applied to automatically correct
107 the laser wavelength.

108 Owing to the failure of the reference cell in this campaign, the NO mixing ratios injected into the HO₂ detection cell were
109 set to be higher than that in other campaigns in China because the HO₂ cell needed to be used as a reference cell to correct
110 laser wavelength. In this campaign, NO mixing ratios were switched between 25 ppm (low NO mode) and 50 ppm (high NO
111 mode). We calculated the HO₂-to-OH conversion efficiencies under the two different NO concentrations by calibrating the
112 PKU-LIF system. HO₂-to-OH conversion efficiencies in low NO mode ranged within 80%-95%, while those in high NO mode
113 reached 100%, demonstrating that the high NO concentration is sufficiently to achieve ~~the complete~~ ~~HO₂-to-OH~~ ~~HO₂-to-OH~~
114 conversion and thus the HO₂ measurement was affected by RO₂ radicals. Prior studies have reported the relative detection
115 sensitivities (α_{RO_2}) for the major RO₂ species, mainly from alkenes, isoprene and aromatics. [Fuchs et al. \(2011\) reported that](#)
116 [the relative RO₂ detection sensitivities are approximately constant when the NO concentration is so high that HO₂ conversion](#)
117 [in the detection is nearly complete. Thus, when the HO₂-to-OH conversion efficiencies reach 100%, the relative RO₂ detection](#)

带格式的: 字体: 10 磅

带格式的: 字体: 10 磅

118 sensitivities reported by Fuchs et al. (2011) and Lu et al. (2012) can be used for the correction of HO₂ concentrations, when
119 the HO₂-to-OH conversion efficiencies reach 100% (Fuchs et al., 2011; Lu et al., 2012; Lu et al., 2013). Herein, only the HO₂
120 observations in high NO mode were chosen and they were denoted as [HO₂], which was the sum of the true HO₂ concentration
121 and a systematic bias from the mixture of RO₂ species *i* which were detected with different relative sensitivities $\alpha_{RO_2}^i$, as
122 shown in Eq. (1) (Lu et al., 2012). The true HO₂ concentration was difficult to be calculated because the observed
123 concentrations of RO₂ concentration measurements and their speciation were not available. Herein, we simulated the HO₂ and
124 HO₂* concentrations by the model, and the RO₂ interference yields which was/were used for correction were the modeled
125 values reported by Lu et al. (2012) in the PRIDE-PRD2006 campaign in which the HO₂-to-OH conversion efficiencies also
126 reached 100% due to the injection of pure NO in the HO₂ detection cell. The interference from RO₂ radicals was estimated to
127 be the difference between the modeled HO₂ and HO₂* concentrations. Overall, the measurement uncertainties of OH and HO₂*
128 radicals were 11% and 15%, respectively, as shown in Table S1 in the Supplementary Information.

$$129 \quad [HO_2] = [HO_2] + \sum(\alpha_{RO_2}^i \times [RO_2]_i) \quad (1)$$

130 Additionally, prior studies reported that OH measurement might be affected by the potential interference, when the sampled
131 air contained ozone, alkenes and BVOCs (Mao et al., 2012; Fuchs et al., 2016; Novelli et al., 2014), indicating the
132 environmental conditions are important to the production of interference. The pre-injector is usually used to test the potential
133 OH interference, and has been applied to our PKU-LIF system to quantify the possible interferences for several campaigns,
134 including the campaigns conducted at the Wangdu, Heshan, Huairou, Taizhou and Chengdu sites (Tan et al., 2017; Tan et al.,
135 2019; Tan et al., 2018; Yang et al., 2021; Ma et al., 2022b). No significant internal interference was found in the prior studies,
136 demonstrating the accuracy of the PKU-LIF system has been determined for several times. Moreover, to further explore the
137 potential interference in this campaign, we compared the major environmental conditions, especially O₃, alkenes and isoprene,
138 between Shenzhen and Wangdu sites, as shown in the Supplementary Information. The results indicated that the environmental
139 condition in Shenzhen was less conducive to generating interference than that in Wangdu, and the details were presented in
140 the Supplementary Information. Besides the environmental conditions, the prior studies reported that the product of the reaction
141 of RO₂ with OH, trioxides (ROOOH), might lead to an OH interference signal. The reactions of RO₂ radicals with OH radicals
142 might be competitive with other sinks for RO₂ radicals (Fittschen, 2019; Fittschen et al., 2019; Berndt et al., 2022). However,
143 Fittschen et al. (2019) reported that the OH interference signals might come from the ROOOH heterogeneous decomposition
144 on the walls of the FAGE cell or the entrance nozzle, but they also noted that the ROOOH interference is highly dependent on
145 the design and measurement conditions of different FAGE instruments. Therefore, we integrated the reactions of the ROOOH
146 production and destruction into the base model herein, with the ROOOH production rate constant of $1.5 \times 10^{-10} \text{ cm}^3 \text{ s}^{-1}$ and the
147 destruction rate constant of 10^{-4} s^{-1} (the details are presented in the Supplementary Information) (Fittschen et al., 2019). Figure.
148 S1 (a) presents the modeled ROOOH concentrations during this campaign, with a maximum of about $4.4 \times 10^9 \text{ cm}^{-3}$. The

带格式的: 字体: 10 磅

带格式的: 下标

带格式的: 下标

149 correlation of the modeled ROOOH concentrations and the ratios of OH observations to OH simulations, and the correlation
150 of the modeled ROOOH concentrations and the difference between OH observations and simulations both demonstrated that
151 no significant relevance between ROOOH and the underestimation of OH radicals, as shown in Fig. S1 (b-c). Additionally, the
152 ROOOH values modeled in our another campaign (Taizhou, 2018) were comparable to or even slightly higher than the
153 simulations in this study, and the chemical modulation tests in Taizhou confirmed the ROOOH is not a significant OH
154 interference in our PKU-LIF system (Ma et al., 2022b). Overall, the OH interference during this campaign was negligible
155 according to the analysis of the behavior of PKU-LIF system in previous campaigns, the comparison of environmental
156 conditions between this campaign and Wangdu campaign, and the exploration of the impact of ROOOH on the discrepancy of
157 OH observations and simulations. However, we should acknowledge that the unmeasured interference might have an effect on
158 radical measurement. More precise chemical modulation tests are needed in the future

159

160 **2.3 Closure experiment**

161 As an effective tool to explore the atmospheric radical chemistry, the radical closure experiment can investigate the state-of-
162 the-art chemical mechanism because of the extremely short lifetime of radicals (Stone et al., 2012; Lu et al., 2019). A zero-
163 dimensional box model was used to conduct the radical closure experiment, and the overall framework was reported by Lu et
164 al. (2019). In this work, we conducted the radical closure experiment based on the Regional Atmospheric Chemical Mechanism
165 updated with the latest isoprene chemistry (RACM2-LIM1), as Tan et al. (2017) described in detail. The model was constrained
166 by the measured meteorological, photolysis frequency, and the critical chemical parameters (CO, NO, NO₂, VOCs, *etc.*). The
167 H₂ and CH₄ mixing ratios were set to 550 ppb and 1900 ppb, respectively. The model was operated in time-dependent mode
168 with a 5-min time resolution, and a 2-d spin-up time was to make the unconstrained species approach the steady state relative
169 to the constrained species.

170 As Lu et al. (2012) described, there are two types of radical closure experiment. One is the comparison of observed and
171 modeled radical concentrations, and the other is the comparison of radical production and destruction rates. The most
172 significant difference between the above is that the latter is conducted with the observed radical concentrations and k_{OH}
173 constrained. The comparison of radical production and destruction rates, which is also called radical experimental budget, can
174 test the accuracy of the state-of-the-art chemistry mechanisms based on the equivalent relationship between the radical
175 production and destruction rates. The production rates of OH, HO₂, and RO₂ radicals are quantified from all the known sources.
176 The destruction rates of HO₂ and RO₂ radicals are the sum of the known sinks, while the OH destruction rate can be directly
177 calculated as the product of the observed OH concentrations and the observed k_{OH} (Tan et al., 2019; Yang et al., 2021). The OH
178 destruction rate is the total sinks of OH radicals because of the direct k_{OH} observation, and thus the discrepancy between the
179 OH destruction and production rates denotes the missing OH sources. The detailed reactions and the reaction rate constants

180 related to OH, HO₂, and RO₂ radicals can be found in Tan et al. (2019) and Yang et al. (2021).

181 2.4 AOC evaluation

182 The life time of the trace gases is controlled not only by the oxidant concentration but also by its second-order rate constant,
183 so the atmospheric oxidation capacity (AOC) proposed by Geyer et al. (2001) is most suitable to evaluate the relative
184 importance of each oxidant (Elshorbany et al., 2009). AOC is the core driving force of complex air pollution, and determines
185 the removal rate of trace gases and the production rates of secondary pollutants (Liu et al., 2021). As an effective indicator for
186 atmospheric oxidation intensity, the evaluation of AOC can provide crucial information on the atmospheric composition of
187 harmful and climate forcing species (Elshorbany et al., 2009). AOC is defined as the sum of the respective oxidation rates of
188 the pollutants via reactions with oxidants (Elshorbany et al., 2009;Geyer et al., 2001;Zhu et al., 2020). According to the
189 definition of AOC, it can be calculated by the Eq. (2).

$$190 \text{ AOC} = \sum_i k_{Y_i}[Y_i][X] \quad (2)$$

191 where Y_i are the pollutants (CO, CH₄, and VOCs), X are the main atmospheric oxidants (OH, O₃, NO₃), and k_{Y_i} is the bi-
192 molecular rate constant for the reaction of Y_i with X . AOC includes all combination of pollutants Y and oxidants X . The
193 higher AOC, the higher removal rate of the atmospheric pollutants, and thus the higher production rate of secondary pollutants
194 (Yang et al., 2020b). Simultaneous measurements of OH and the key trace gases are available in the study. NO₃ concentration
195 could be simulated by the box model with the observed parameters constrained.

196 3. Results

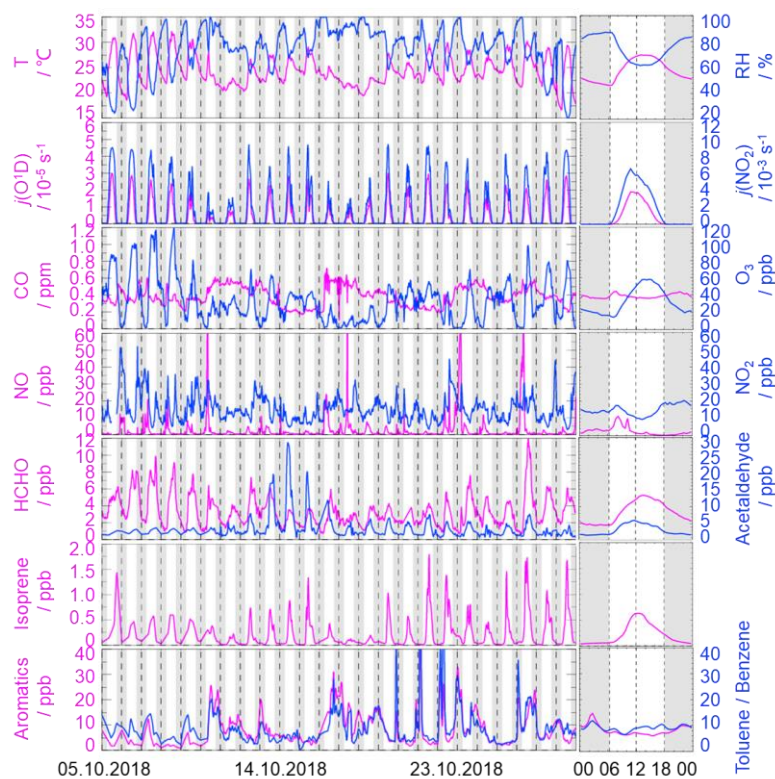
197 3.1 Meteorological and chemical conditions

198 Figure 2 gives an overview of the meteorological and chemical parameters from 05 October to 28 October 2018, when OH
199 and HO₂ radicals were measured. The diurnal variations of the temperature (T), relative humidity (RH), $j(\text{O}^1\text{D})$, and $j(\text{NO}_2)$
200 followed a regular pattern from day to day. The overall meteorological conditions were characterized by high temperature
201 (about 20~30 °C), high relative humidity (60~80%), and intensive radiation with $j(\text{O}^1\text{D})$ up to $2.0 \times 10^{-5} \text{ s}^{-1}$ and $j(\text{NO}_2)$ up to
202 $6.0 \times 10^{-3} \text{ s}^{-1}$. The relative humidity and photolysis-frequency in this autumn campaign were similar to those in the summer
203 campaign conducted in Chengdu (Yang et al., 2021). The temperature in this campaign was lower than that in Chengdu, but
204 similar to that in the autumn campaign in Heshan located in PRD as well (Tan et al., 2019;Yang et al., 2021).

205 The concentration of CO showed a weak diurnal variation, indicating there was the non-obvious accumulation of
206 anthropogenic emissions on a regional scale. NO concentration peaked at 12 ppb during morning rush hour when the traffic
207 emission was severe, and thereafter, O₃ concentration started to increase with the decreasing of NO concentration. The maxima
208 of O₃ hourly concentration were high up to 120 ppb. According to the updated National Ambient Air Quality Standard of China

209 (GB3095-2012), O₃ concentration exceeded the Class-II limit values (hourly averaged limit 93 ppb) on several days (6, 7, 8,
210 and 26 October) when the environmental condition was characterized by high temperature and low relative humidity. NO₂
211 concentration was high at night because of the titration effect of O₃ with NO.

212 Along with the high O₃ concentration on 6, 7, 8, and 26 October, high HCHO concentration was also recorded during the
213 corresponding periods, indicating HCHO was mainly produced as secondary pollutants because of the active
214 photochemistry in this campaign. Isoprene, which is mostly derived from biogenic emissions and mainly affected by
215 temperature, peaked around noontime. Tan et al. (2019) reported the median concentration of HCHO and isoprene
216 concentrations were 6.8 ppb and 0.6 ppb during 12:00-18:00 at Heshan site. Similarly, the median concentration of HCHO and
217 isoprene concentrations in this study were 4.9 ppb and 0.4 ppb during the corresponding periods, respectively. As a proxy for
218 traffic intensity, the toluene to benzene ratio (T/B), which is below 2, means the traffic emissions are the major sources of
219 VOCs (Brocco et al., 1997). In this campaign, the T/B gradually dropped from 07:00 until it reached the minimum value at
220 09:00, indicating traffic emission contributed more to VOCs during morning rush hour than during other periods. However,
221 the T/B values, which varied within a range of 7-12, were above 2, and thus VOCs emission during this campaign was mainly
222 from other sectors such as those involving solvent evaporation.



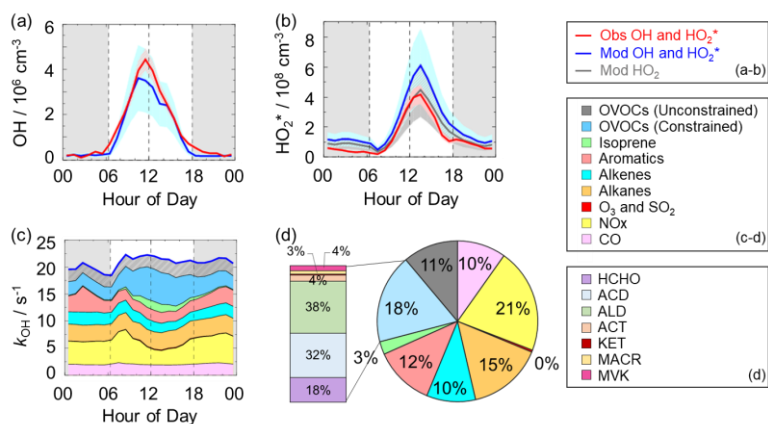
223
 224 **Figure 2: Timeseries and diurnal profiles of the observed meteorological and chemical parameters in the STORM campaign. The**
 225 **grey areas denote nighttime.**

226 Moreover, we compared the environmental conditions between the Backgarden (rural site), Heshan (suburban site), and
 227 Shenzhen (urban site) campaigns conducted in PRD in Table S3 in the Supplementary Information. No significant discrepancy
 228 in temperature was found in the Shenzhen and Heshan campaigns, which were both conducted in autumn. The temperature in
 229 the Backgarden campaign conducted in summer was higher than those in Shenzhen and Heshan. The relative humidity in
 230 Shenzhen and Backgarden was higher than that in Heshan. Compared to the chemical conditions in the Heshan campaign
 231 conducted in autumn as well, the concentrations of CO, NO, NO₂, HONO, alkenes, aromatics, and HCHO in Shenzhen were
 232 lower, which might be because there were no significant local pollution sources nearby at the Shenzhen site although it was
 233 an urban site. However, the concentration of O₃ which is the typical secondary pollutant in Shenzhen was higher than that in
 234 Heshan. Compared to the environmental conditions in Heshan, the higher O₃ concentration in Shenzhen might benefit from
 235 the weather condition which was characterized by the stronger solar radiation and slightly higher temperatures.

3.2 Observed and modeled OH and HO₂ radicals

The OH and HO₂ radicals were measured during 05-28 October 2018. The timeseries of the observed and modeled HOx concentrations are displayed in Fig. S2 (a-b) in the Supplementary Information. Data gaps were caused by the rain, calibration, and maintenance. The daily maxima of the observed OH and HO₂ concentrations varied in the range of $(2-9) \times 10^6 \text{ cm}^{-3}$ and $(2-14) \times 10^8 \text{ cm}^{-3}$, respectively. As in previous campaigns, the largest OH concentrations appeared around noontime and showed a high correlation with $j(\text{O}^1\text{D})$, a proxy for the solar UV radiation driving much of the primary radical production (Tan et al., 2019).

Figure 3 (a-b) shows the diurnal profiles of the observed and modeled HOx concentrations. The HOx radicals showed similar diurnal behavior to those reported in other campaigns (Ma et al., 2019a; Tan et al., 2017; Tan et al., 2019; Tan et al., 2018; Yang et al., 2021). The observed OH and HO₂ concentrations reached a maximum around 12:00 and 13:30, respectively. The diurnal maxima of the observed and modeled OH concentrations were $4.5 \times 10^6 \text{ cm}^{-3}$ and $3.5 \times 10^6 \text{ cm}^{-3}$. Compared to the other campaigns conducted in PRD (Backgarden and Heshan), the diurnal maximum of the observed OH concentration in Shenzhen was equal to that observed in Heshan, and much lower than that observed in Backgarden where the observed OH concentration was nearly $15 \times 10^6 \text{ cm}^{-3}$ (Hofzumahaus et al., 2009; Tan et al., 2019). The higher OH concentration at Backgarden site was closely correlated to the stronger solar radiation, as shown in Table S3 in the Supplementary Information. The diurnal observed and modeled OH concentrations agreed within their 1- σ uncertainties of measurement and simulation (11% and 40%). However, when the NO mixing ratio (Fig. 2) dropped from 10:00 gradually, a systematic difference existed, with the observed OH concentration being about $1 \times 10^6 \text{ cm}^{-3}$ higher than the modeled OH concentration. The OH concentrations observed in the environments with low NO levels were underestimated by the state-of-the-art models at Backgarden (summer) and Heshan (autumn) sites in PRD as well, and the OH underestimation was identified to be universal at low NO conditions in China (Lu et al., 2013; Lu et al., 2012; Ma et al., 2019a; Tan et al., 2017; Yang et al., 2021; Ma et al., 2022b). The reason on OH underestimation was further discussed in Section 4.1.



259

260

261

262

263

264

265

Figure 3: (a-b) The diurnal profiles of the observed and modeled OH, HO₂* and HO₂ concentrations. (c) The diurnal profiles of the modeled k_{OH}. (d) The composition of the modeled k_{OH}. The red areas in (a-b) denote 1-σ uncertainties of the observed OH and HO₂* concentrations. The blue areas in (a-b) denote 1-σ uncertainties of the modeled OH and HO₂* concentrations, and the dark grey area in (b) denotes 1-σ uncertainties of the modeled HO₂ concentrations. The grey areas in (a-c) denote nighttime. ACD denotes acetaldehydes, ALD denotes the C3 and higher aldehydes, ACT and KET denote acetone and ketones. MACR and MVK denote methacrolein and methyl vinyl ketone.

266

267

268

269

270

271

272

273

274

275

276

277

278

279

280

281

The diurnal maximum of the observed HO₂*, the modeled HO₂* and the modeled HO₂ concentrations were $4.2 \times 10^8 \text{ cm}^{-3}$, $6.1 \times 10^8 \text{ cm}^{-3}$, and $4.4 \times 10^8 \text{ cm}^{-3}$, respectively. The difference between the modeled HO₂* and HO₂ concentrations can be considered a modeled HO₂ interference from RO₂ (Lu et al., 2012). The RO₂ interference was small in the morning, while it became larger in the afternoon. It ranged within 23%-28% during the daytime (08:00-17:00), which was comparable with those at the Backgarden and Yufa sites in China, Borneo rainforest in Malaysia (OP3 campaign, aircraft), and UK (RONOCO campaign, aircraft) (Lu et al., 2012; Lu et al., 2013; Jones et al., 2011; Stone et al., 2014). The observed HO₂* was overestimated by the model, indicating the HO₂ heterogeneous uptake might have a significant impact during this campaign. The diurnal maximum of HO₂* concentration observed in Shenzhen was much lower than those observed at the Yufa and Backgarden sites (Hofzumahaus et al., 2009; Lu et al., 2012; Lu et al., 2013). The high modeled HO₂/OH ratio around noontime (11:00-15:00), which was about 138, was found in this campaign, which was higher than those at the Backgarden and Chengdu sites (Yang et al., 2021; Hofzumahaus et al., 2009). High HO₂/OH ratio is normally found only in clean air at low NO_x (= NO + NO₂) concentrations of NO_x (Hofzumahaus et al., 2009; Stevens et al., 1997). As an indicator that can reflect the interconversion reaction between HO₂ and OH, the conversion efficiency in this campaign was slightly slower than those at the Backgarden and Chengdu sites.

带格式的: 下标

3.3 OH reactivity

k_{OH} is the pseudo-first-order loss rate coefficient of OH radicals, and it is equivalent to the reciprocal OH lifetime (Fuchs et

282 al., 2017; Lou et al., 2010; Yang et al., 2019). In this campaign, k_{OH} was measured only for several days (05-19 October 2018)
283 by the LIP-LIF system, which has been reported in the previous study (Liu et al., 2019). The timeseries of the observed and
284 modeled k_{OH} during 05-19 October 2018 are presented in Fig. S3 in the Supplementary Information. A good agreement between
285 the observed k_{OH} and modeled k_{OH} within the uncertainties was achieved, and thus the model can be believed to reproduce the
286 observed k_{OH} values within the whole campaign. Moreover, to reflect the k_{OH} in the whole campaign, the modeled values were
287 shown in the k_{OH} diurnal profiles (Fig. 3 (c)) and k_{OH} timeseries (Fig. S2 (c)) during 05-28 October 2018. The modeled k_{OH}
288 showed a weak diurnal variation and varied from 18 s^{-1} to 22 s^{-1} . Compared to the k_{OH} variation in Shenzhen, the k_{OH} observed
289 at Backgarden and Heshan sites in PRD showed a stronger diurnal variation, with a minimum value at around noontime and a
290 maximum value at daybreak. Additionally, the k_{OH} values in this campaign were lower than those at Backgarden ($20\text{-}50 \text{ s}^{-1}$)
291 and Heshan ($22\text{-}32 \text{ s}^{-1}$) sites (Lou et al., 2010; Tan et al., 2019). Similar with the good agreement between the observed and
292 modeled k_{OH} during the several days in Shenzhen, the observed k_{OH} in Backgarden was matched well with the modeled k_{OH}
293 which has included the OVOCs reactivity. In terms of the k_{OH} in Heshan, Tan et al. (2019) reported that only half of the
294 observed k_{OH} was explained by the calculated k_{OH} which was calculated from the measured trace gas concentrations. The
295 missing k_{OH} in Heshan was likely caused by unmeasured VOCs, demonstrating the necessary to measure more abundant VOCs
296 species, especially OVOCs species.

297 As shown in Fig. 3 (d), we presented the composition of modeled k_{OH} . The inorganic compounds contributed approximately
298 31% to k_{OH} , in which the CO and NO_x reactivity accounted for 10% and 21%, respectively. The NO_x reactivity was displayed
299 versus time, with a maximum during the morning peak. The peak concentration during the morning peak was associated with
300 traffic emissions.

301 Compared with the inorganic reactivity, the larger fraction of k_{OH} came from the VOCs group, with a contribution of 69%
302 to k_{OH} . The contribution of alkanes, alkenes, and aromatics were 15%, 10%, and 12%, respectively. The isoprene reactivity
303 related to temperature was mainly concentrated during the daytime, whereas the aromatics reactivity at night was higher. As
304 for the OVOCs species, we measured several OVOCs species, including HCHO, acetaldehydes (ACD) and higher aldehydes
305 (ALD), acetone (ACT), ketones (KET) and isoprene oxidation products (methacrolein (MACR) and methyl vinyl ketone
306 (MVK)), and thus we constrained these species in the model. The constrained OVOCs species accounted for 18% in the total
307 k_{OH} , where HCHO, ACD, and ALD were the major contributors, with contributions of 18%, 32%, and 38% to the constrained
308 OVOCs, respectively. The contribution of aldehydes in this study (16%) was larger than that in Beijing (Whalley et al., 2021)
309 and smaller with that in Wangdu (Fuchs et al., 2017). The remaining reactivity was attributed to the unconstrained OVOCs
310 reactivity, which came from the model-generated intermediate species (glyoxal, methylglyoxal, methyl ethyl ketone, methanol,
311 etc.), with a contribution of 11% to the total k_{OH} . Large fraction of OVOCs reactivities in k_{OH} was also found in some previous
312 studies (Lou et al., 2010; Lu et al., 2013; Fuchs et al., 2017; Whalley et al., 2021). About 50% of k_{OH} was explained by OVOCs
313 at Backgarden site, and HCHO, ACD and ALD, and oxygenated isoprene products were the most important OH reactants in

314 OVOCs, with a contribution of 30-40%, and other 10-20% came from other oxygenated compounds (ketones, dicarbonyl
315 compounds, alcohols, hydroperoxides, nitrates etc.) (Lou et al., 2010). HCHO, ACD, MVK, MVCR and glyoxal accounted for
316 one-third of the total k_{OH} at Wangdu site (Fuchs et al., 2017). The large unconstrained OVOCs reactivity indicated it is
317 necessary to measure more VOCs species in the future.

318 4. Discussion

319 4.1 Radical closure experiment

320 In this study, we conducted OH radical closure experiment which is called OH experimental budget as well. As discussed in
321 Section 3.3, it is believed that the model can reproduce the observed k_{OH} . Herein, to conduct the OH experiment budget in the
322 whole campaign, we used the modeled k_{OH} to calculate the OH destruction rate because the k_{OH} was only measured on several
323 days. The diurnal profiles of OH production and destruction rates, and the compositions of OH production rate were displayed
324 in Fig. 4, with maxima of 14 ppb h⁻¹ and 17 ppb h⁻¹ around noontime, respectively. The OH production rate from known sources
325 is quantified from the primary sources (photolysis of HONO, photolysis of O₃, ozonolysis of alkenes) and secondary sources
326 (dominated by HO₂ + NO, and HO₂ + O₃). The primary and secondary sources accounted for 78% and 22% of the total
327 calculated production rate, respectively. Similar with the prior studies, the largest fraction of OH production rate came from
328 HO₂ + NO, with a contribution up to 76% of the known OH production rate. As the major primary OH sources, the HONO
329 and O₃ photolysis contributed 13% and 7% to the total calculated OH production rate, respectively.

330 The OH production rate matched well with the destruction rate only in the early morning to about 10:00. Thereafter, the OH
331 destruction rate was larger than the production rate, which could explain the underestimation of OH concentration by the model.
332 As shown in Fig. 4 (b), the discrepancy between the OH production and destruction rates at around 11:00-15:00, which was
333 approximately of (3.1~4.6) ppb h⁻¹, cannot be explained by the combined experimental uncertainties. The discrepancy was
334 attributed to the missing OH sources because k_{OH} was constrained in this study. The biggest additional OH source was
335 approximately 4.6 ppb h⁻¹, which occurred at about 12:00, when the OH production and destruction rates were 11.9 ppb h⁻¹
336 and 16.5 ppb h⁻¹, respectively. The unknown OH source accounted for about one third of the total OH production rate,
337 indicating the exploration of missing OH source was significant to study the radical chemistry. It is noted that the OH
338 production rate was overestimated because we used HO₂ concentrations instead of HO₂ concentrations here. Thus, the
339 missing OH source was the lower limit here, demonstrating more unknown OH sources need to be further explored. Details
340 on unknown OH sources are given below (Sect. 4.2).

341

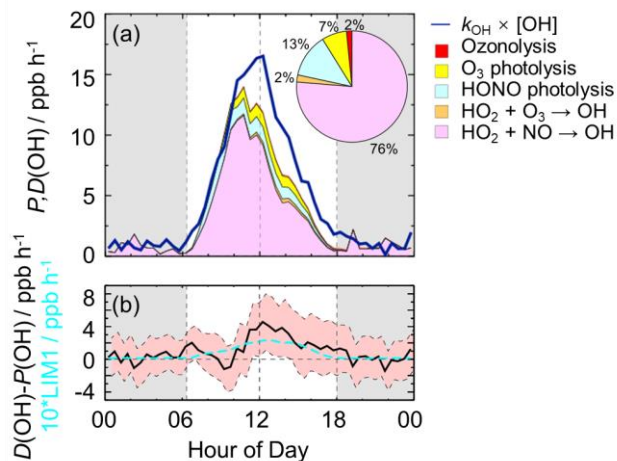


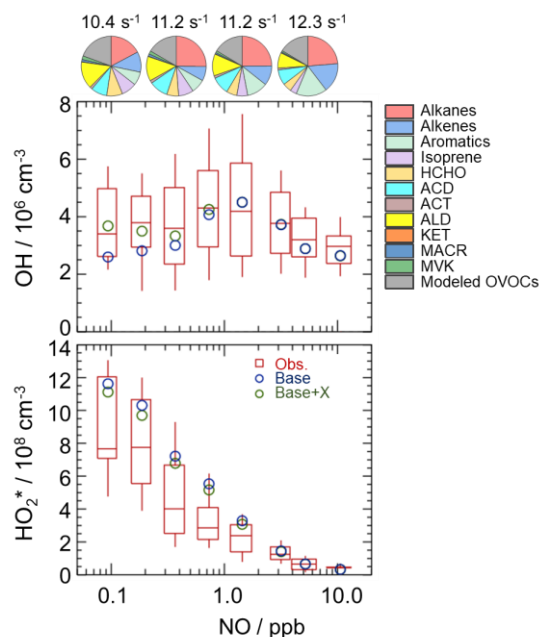
Figure 4: (a) The diurnal profiles of OH production and destruction rates and the proportions of different known sources in the calculated production rate during the daytime. The blue line denotes the OH destruction rate, and the colored areas denote the calculated OH production rates from the known sources. (b) The missing OH source which was the discrepancy between the OH destruction and production rates, and the OH production rate which was ten times the production rate derived from LIM1 mechanism. The red shaded areas denote the combined uncertainty from the experimental errors of the measured quantities (Table S1) and the reaction rate coefficients. The grey areas denote nighttime.

4.2 Radical chemistry in low NO regime

4.2.1 Influencing factors of OH underestimation

As analyzed in Sect. 4.1, the underestimation of OH concentration was attributable to the missing OH source. It is necessary to explore the influencing factor for gaining further insight into the missing source. Scientists reported that more significant OH underestimation would appear with the decreasing NO concentration and increasing isoprene concentration (Lu et al., 2012; Ren et al., 2008; Hofzumahaus et al., 2009; Lelieveld et al., 2008; Whalley et al., 2011; Tan et al., 2017; Yang et al., 2021). Herein, we further explored the effect of NO concentration on missing OH source. The NO dependence on observed and modeled HOx concentrations and the NO dependence on HOx observed-to-modeled ratios were illustrated in Fig. 5 and Fig. S4. The OH concentrations were normalized by the averaged $j(\text{O}^1\text{D})$ to eliminate the influence of radiation on radicals. The OH concentration showed an increasing trend with the increase of NO concentrations in low NO regime (below 1 ppb) due to the increased OH radicals from propagation via peroxy reactions with NO, and then decreased with the increase of NO concentrations in high NO regime (above 1 ppb) due to the OH loss by the reactions via NO_2 (Ehhalt, 1999). The base model can reproduce the observed OH concentration in high NO regime, while-and underestimate OH concentration in low NO regime. As for HO_2^* radicals, the observed and modeled HO_2^* concentrations decreased with the increase of NO

364 concentrations. The model overestimated the observations, indicating that the heterogeneous uptake might make a significant
 365 role in HO₂ sinks in this campaign. Overall, NOx (=NO+NO₂) plays a crucial role in radical chemistry due to their impact
 366 of NO on radical propagation and termination reactions.



367
 368 **Figure 5: NO dependence on OH and HO₂ radicals.** The red box-whisker plots give the 10%, 25%, median, 75%, and 90% of the
 369 HOx observations. The blue circles show the median values of the HOx simulations by the base model, and the green circles show
 370 the HOx simulations by the model with X mechanism. Total VOCs reactivity and their organic speciation are presented by pie charts
 371 at the different NO intervals at the top. Only daytime values and NO concentration above the detection limit of the instrument were
 372 chosen. ACD and ACT denote acetaldehyde and acetone, respectively. ALD denotes the C3 and higher aldehydes. KET denotes
 373 ketones. MACR and MVK, which are both the isoprene oxidation products, denote methacrolein and methyl vinyl ketone,
 374 respectively.

375 To further explore the influencing factors of OH underestimation, we presented the speciation VOCs reactivity under the
 376 different NO intervals, as shown in Fig. 5 and Table S4 in the Supplementary Information. The isoprene reactivity and total
 377 OVOCs reactivity (the sum of HCHO, ACD, ACT, ALD, KET, MACR, MVK and the modeled OVOCs) increased with the
 378 decrease of NO concentrations, while the anthropogenic VOCs reactivity (alkanes, alkenes and aromatics) was higher in high
 379 NO regime. Additionally, the O₃ concentration in low NO regime was significantly higher than those in high NO regime, and
 380 the temperature was slightly higher in low NO regime, demonstrating the photochemistry was more active in low NO regime
 381 in this campaign. Overall, the photochemistry and composition of VOCs reactivity, especially the isoprene and OVOCs species
 382 (mainly HCHO, ACD, ALD and the modeled OVOCs), might closely impact the missing OH sources.

4.2.2 Quantification of missing OH sources

Hofzumahaus et al. (2009) proposed an existence of a pathway for the regeneration of OH independent of NO, including the conversions of $\text{RO}_2 \rightarrow \text{HO}_2$ and $\text{HO}_2 \rightarrow \text{OH}$ by a numerical species called X. With a retrospective analysis, the unclassical OH recycling pathway was identified to be universal at low NO conditions in China. The amount of X varies with environmental conditions, and the X concentrations were 0.85 ppb, 0.4 ppb, 0.1 ppb, 0.4 ppb, 0.1 and 0.25 ppb at Backgarden, Yufa, Wangdu, Heshan, Taizhou, and Chengdu sites (Hofzumahaus et al., 2009; Lu et al., 2012; Lu et al., 2013; Tan et al., 2017; Yang et al., 2021; Ma et al., 2022b).

In this study, we tested this unclassical X mechanism. Good agreement between observations and simulations of OH radicals was achieved when a constant mixing ratio of 0.1 ppb of X was added into the base model. As shown in Fig. 5, the model with X mechanism agreed with the observed OH concentrations even at low NO conditions. Unclassical OH recycling was identified again in this study. ~~However~~ Nevertheless, X is an artificial species that behaves like NO, and thus the nature of X is still unknown to us. Compared to the Shenzhen site, the required X concentration in the Backgarden and Heshan sites in PRD was higher, which might be affected by the different air masses in the three sites. The k_{OH} ~~in~~ at Shenzhen site was much lower than those at Backgarden and Heshan sites (Lu et al., 2013), and a weaker diurnal variation of k_{OH} in Shenzhen was observed. Under the influence of the East Asian monsoon, the prevailing wind for PRD area is mostly southerly during the summer months and mostly northerly during the winter months (Fan et al., 2005; Zhang et al., 2008). The Backgarden site is located in Guangzhou, and the Heshan site is located in Jiangmen. The two cities are along the north-south axis, and thus the air masses of the Backgarden and Heshan sites are intimately linked with each other, while the air mass in Shenzhen is more similar to Hongkong (Zhang et al., 2008). Compared to the VOCs reactivity in the air mass at Backgarden and Yufa sites reported by Lu et al. (2013), lower isoprene reactivity and OVOCs reactivity were observed in Shenzhen site. As discussed in Section 4.2.1, the OH underestimation might be closely related to the composition of VOCs reactivity. Therefore, further exploration of this unclassical OH recycling is needed to improve our understanding of radical chemistry, especially the mechanisms related to isoprene and OVOCs.

As for the potential influence of isoprene and OVOCs on the missing OH source, RO_2 isomerization reactions have also been shown to be of importance for the atmospheric fate of RO_2 from isoprene (Peeters et al., 2009; Peeters et al., 2014). The latest isoprene isomerization mechanism, which is called LIM1, has been coupled into our current base model. However, LIM1 mechanism was not included in the OH experimental budget which was conducted with the observations constrained, as shown in Section 4.1. Herein, we evaluated the contribution of LIM1 mechanism to the missing OH sources, as shown in Fig. 4 (b). LIM1 mechanism can explain approximately 7% of the missing OH sources during 10:00-16:00, when the missing OH production rate and the OH production rate derived from LIM1 mechanism were 2.47 ppb h^{-1} and 0.17 ppb h^{-1} , respectively.

Additionally, prior studies also reported that OH regeneration might be achieved from the oxidation of MACR and MVK,

414 which are the major first-generated products of isoprene (Fuchs et al., 2018;Fuchs et al., 2014). As a potential explanation for
 415 the high OH concentration, the impacts of MACR and MVK oxidation were evaluated here. The modification of MACR
 416 oxidation scheme added the H-migration reactions of MACR oxidation products (Fuchs et al., 2014). The modification of
 417 MVK oxidation scheme added the reactions of MVK oxidation products with HO₂ radicals and the H-migration reactions of
 418 MVK oxidation products (Fuchs et al., 2018). As presented in Fig. S5 in the Supplementary Information, no significant of the
 419 MACR and MVK oxidation schemes was found in this campaign.

420 Overall, a large part of missing OH sources was not explained by the isoprene chemistry. In the future, the impact of OVOCs
 421 species which was another potential OH source on missing OH sources need to be further evaluated.

422 4.3 HO₂ heterogeneous uptake

423 The HO₂^{*} overestimation was identified by comparing the observed and modeled HO₂^{*} concentrations in Sect. 3.2 and Sect.
 424 4.2.1. The HO₂ heterogeneous uptake has been proposed to be a potential sink of HO₂ radicals, and thus could influence the
 425 radical chemistry and the formation of secondary pollution, especially in high-aerosol environments (Song et al., 2021;Song
 426 et al., 2022;Tan et al., 2020;Kanaya et al., 2000;Kanaya et al., 2007;Li et al., 2019). The impact of HO₂ uptake chemistry on
 427 radical concentration is different under different environmental conditions (Whalley et al., 2015;Mao et al., 2010;Li et al.,
 428 2019). To evaluate the contribution of HO₂ uptake chemistry to radical concentrations in this study, we coupled HO₂
 429 heterogeneous uptake into the base model (RACM2-LIM1) and conducted three sensitivity experiments, as shown in R1 and
 430 Eq. (3).



$$432 k_{\text{HO}_2+\text{aerosol}} = \frac{\gamma \cdot \text{ASA} \cdot v_{\text{HO}_2}}{4} \quad (3)$$

433 where ASA [μm² cm⁻³], which represents the aerosol surface area concentration, can be estimated by multiplying the mass
 434 concentration of PM_{2.5} [μg m⁻³] by 20 here because there were no direct ASA observations in this campaign (Chen et al.,
 435 2019;Wang et al., 2017b). v_{HO_2} , which can be calculated by Eq. (4), refers to the mean molecular velocity of HO₂ with a unit
 436 of cm s⁻¹.

$$437 v_{\text{HO}_2} = \sqrt{\frac{8 \cdot R \cdot T}{0.033 \cdot \pi}} \quad (4)$$

438 where T [K] and R [J mol⁻¹ K⁻¹] denote the ambient temperature and gas constant. γ , the HO₂ effective uptake coefficient,
 439 parameterizes the influence of some processes (Tan et al., 2020). γ varies in the highly uncertain range of 0-1 (Song et al.,
 440 2022), and is the most critical parameter to impact HO₂ uptake chemistry. Only several observations of γ have been reported
 441 (Taketani et al., 2012;Zhou et al., 2021;Zhou et al., 2020). The measured γ at the Mt. Tai site and Mt. Mang site were 0.13-
 442 0.34 and 0.09-0.40, respectively (Taketani et al., 2012). The average value of the measured γ was 0.24 in Kyoto, Japan in the

443 summer of 2018 (Zhou et al., 2020). Zhou et al. (2021) reported the lower-limit values for median and average values of the
 444 measured γ were 0.19 and 0.23 ± 0.21 in Yokohama, Japan in the summer of 2019. Additionally, Li et al. (2018) set 0.2 as the
 445 value of γ in the model, and Tan et al. (2020) calculated the γ of 0.08 ± 0.13 by the analysis of the measured radical budget in
 446 Wangdu.

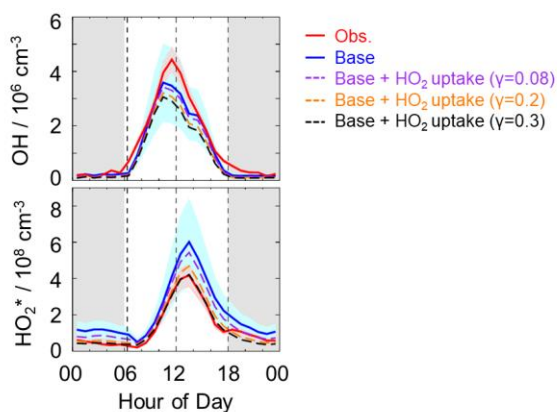
447 Here, we applied the two γ (0.2 and 0.08), which have been used in the model, to evaluate the impact of HO_2 uptake on
 448 radical concentrations, as shown in Fig. 6. The modeled HO_2^* cannot match well with the observations when γ of 0.08 and 0.2
 449 was set in the model. As the γ increased to approximately 0.3, good agreement between the modeled and observed HO_2^*
 450 concentration was achieved, demonstrating that ~~the a~~ significant heterogeneous uptake might exist in this campaign. It should
 451 be noted that the HO_2 heterogeneous uptake ($\gamma = 0.3$) reduced the modeled OH concentrations by around 20% compared to the
 452 OH simulations in the base model during the daytime (08:00-18:00). Sensitivity tests illustrated that good agreements of OH
 453 observations-simulations and HO_2^* observations-simulations were both achieved when the amount of X changed from 0.1 ppb
 454 to 0.25 ppb and the HO_2 effective uptake coefficient was 0.3, as shown in Fig. S6 in the Supplementary Information. Compared
 455 to the Backgarden and Heshan sites, the amount of X in Shenzhen was still lower despite a significant HO_2 heterogeneous
 456 uptake, which might be closely related to the environmental conditions as discussed in Sect. 4.2.

带格式的: 下标

带格式的: 字体: 10 磅

带格式的: 字体: 10 磅

带格式的: 字体: 10 磅

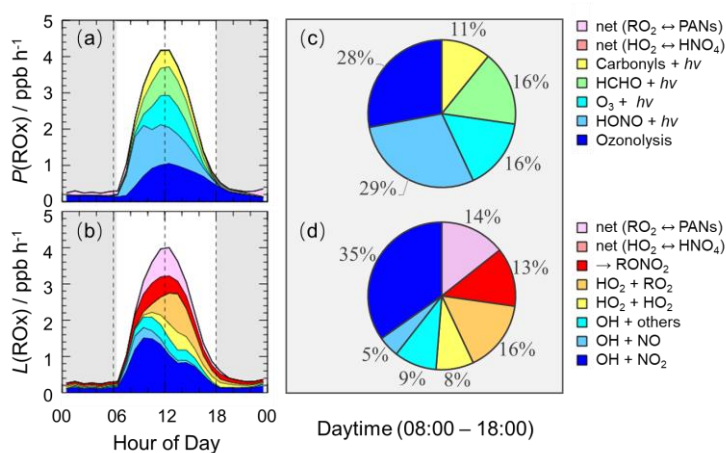


457
 458 **Figure 6: The diurnal profiles of the observed and modeled radical concentrations. The red and blue areas denote 1- σ uncertainties**
 459 **of measured and simulated radical concentrations by the base model, respectively. The orange, purple and black lines denote the**
 460 **simulations by the model which added the HO_2 heterogeneous uptake with different uptake coefficient. The grey areas denote**
 461 **nighttime.**

462 It is noted that the estimated strong influence is speculative because of the uncertainties of measurements and simulations.
 463 Overall, the γ evaluated in this study was comparable with those observed at the Mt. Tai and Mt. Mang in China, and Kyoto
 464 and Yokohama in Japan.

465 **4.4 Sources and sinks of ROx**

466 The detailed analysis of radical sources and sinks was crucial to exploring radical chemistry. The experimental budget for HO₂
 467 and RO₂ radicals could not be conducted because RO₂ was not measured during this campaign. Herein, we showed the
 468 simulated results by the base model. Figure 7 illustrates the diurnal profiles of ROx primary production rate ($P(\text{ROx})$) and
 469 termination rate ($L(\text{ROx})$), and the contributions of different channels during the daytime.



470 **Figure 7: The diurnal profiles of ROx primary production rate (a) and termination rate (b) simulated by the base model, and the**
 471 **contributions of different channels to ROx primary production rate (c) and termination rate (d) during the daytime (08:00-18:00).**
 472 **The grey areas denote nighttime.**
 473

474 The ROx primary production and termination rates were basically in balance for the entire day, with maxima of 4 ppb h^{-1}
 475 around noontime. The ROx primary production rate was similar to those at Heshan (4 ppb h^{-1}) and Wangdu (5 ppb h^{-1}) sites,
 476 but lower than those at Backgarden (11 ppb h^{-1}), Yufa (7 ppb h^{-1}), Taizhou (7 ppb h^{-1}) and Chengdu (7 ppb h^{-1}) sites (Lu et al.,
 477 2013; Lu et al., 2012; Tan et al., 2017; Tan et al., 2019; Yang et al., 2021). During the daytime, the $P(\text{ROx})$ mainly came from
 478 the OH and HO₂ primary production. HONO and O₃ photolysis dominated the OH primary production, and HCHO photolysis
 479 dominated the HO₂ primary production. Thus, $P(\text{ROx})$ was dominated by the photolysis reactions, in which the photolysis of
 480 HONO, O₃, HCHO, and carbonyls accounted for 29%, 16%, 16%, and 11% during the daytime, respectively. In the early
 481 morning, HONO photolysis was the most important primary source of ROx, and the contribution of O₃ photolysis became
 482 progressively larger and was largest at noontime. A large discrepancy between the ratio of HONO photolysis rate to O₃
 483 photolysis rate in summer/autumn and that in winter occurs generally. The vast majority of OH photolysis source is attributed
 484 to HONO photolysis in winter because of the higher HONO concentration and lower O₃ concentration. About half of $L(\text{ROx})$
 485 came from OH termination, which occurred mainly in the morning, and thereafter, radical self-combination gradually became
 486 the major sink of ROx in the afternoon. OH + NO₂, OH + NO, and OH + others contributed 35%, 5%, and 9% to $L(\text{ROx})$,

487 respectively. HO₂ + HO₂ and HO₂ + RO₂ accounted for 8% and 16% in L(ROx).

488 4.5 AOC evaluation

489 AOC controls the abundance of precursors and the production of secondary pollutants (Yang et al., 2020a;Elshorbany et al.,
490 2009), and thus it is necessary to quantify AOC for understanding photochemical pollution. The AOC has been evaluated in
491 previous studies, as shown in Table 1. Overall, the AOC values in summer are higher than those in autumn and winter, and the
492 values at lower latitudes are higher than those at higher latitudes for the same season. The vast majority of AOC in previous
493 studies are evaluated based on the non-observed radical concentrations.

494 **Table 1: Summary of OH concentrations and AOC values reported in previous field campaigns.**

Location	Season, year	Site	Observed or non-observed of OH radicals		AOC / 10 ⁸	References
			observed	of OH radicals	molecules cm ⁻³ s ⁻¹	
Beijing, China	summer, 2018	urban	non-observed	values	0.89 ^a	(Liu et al., 2021)
Beijing, China	summer, 2018	suburban	non-observed	values	0.85 ^a	(Liu et al., 2021)
Beijing, China	winter, 2018	urban	non-observed	values	0.21 ^a	(Liu et al., 2021)
Beijing, China	winter, 2018	suburban	non-observed	values	0.16 ^a	(Liu et al., 2021)
Hongkong, China	summer, 2011	suburban	non-observed	values	2.04 ^{a,b}	(Xue et al., 2016)
Santiago, Chile	summer, 2005	urban	non-observed	values	3.4 ^a	(Elshorbany et al., 2009)
Hong Kong, China	late summer, 2012	coastal	non-observed	values	1.4 ^c	(Li et al., 2018)
Hong Kong, China	autumn, 2012	coastal	non-observed	values	0.62 ^c	(Li et al., 2018)
Hong Kong, China	winter, 2012	coastal	non-observed	values	0.41 ^c	(Li et al., 2018)
Shanghai, China	summer, 2018	urban	non-observed	values	1.0 ^c	(Zhu et al., 2020)
Berlin, Germany	summer, 1998	suburban	non-observed	values	0.14 ^d	(Geyer et al., 2001)
Xianghe, China	autumn, 2019	suburban	non-observed	values	0.49 ^c	(Yang et al., 2020a)
Beijing, China	summer, 2014	urban	non-observed	values	1.7 ^a	(Feng et al., 2021)

495 Note that:

496 ^a Peak values in the diurnal profiles; ^b Values on 25 August 2021; ^c Maximum over a period of time; ^d Maximum on some day.

497 Herein, we explored the AOC in Shenzhen based on the observed radical concentrations for the first time. As illustrated in
498 Fig. 8 (a), the diurnal profile of AOC exhibited a unimodal pattern, which was the same as the diurnal profile of OH
499 concentration and $j(\text{NO}_2)$, with a peak around noontime. The diurnal peak of AOC was 0.75×10^8 molecules cm⁻³ s⁻¹ (11.8 ppb
500 h⁻¹). Comparatively, AOC in this study was comparable to those evaluated in Beijing (summer, 2018) and Hong Kong (autumn,
501 2012) (Li et al., 2018;Liu et al., 2021), but much lower than those evaluated in Hong Kong (summer, 2011) and Santiago

(summer, 2005) (Xue et al., 2016; Elshorbany et al., 2009).

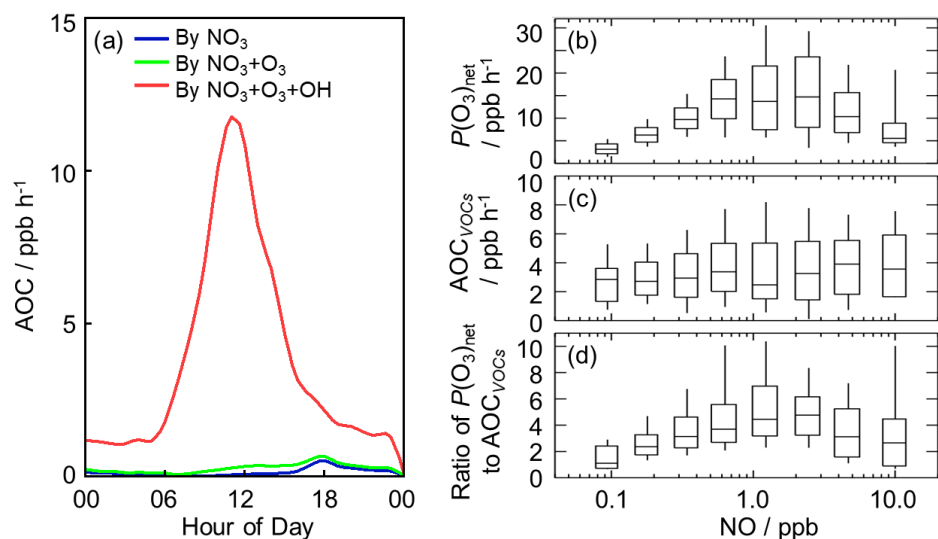


Figure 8: (a) The diurnal profiles of AOC in this campaign. (b) NO dependence on $P(O_3)_{net}$ during the daytime. (c) NO dependence on AOC_{VOCs} during the daytime, and AOC_{VOCs} denotes the atmospheric oxidation capacity only from the VOCs oxidation. (d) NO dependence on the ratio of $P(O_3)_{net}$ to AOC_{VOCs} during the daytime. The box-whisker plots in (b-d) give the 10%, 25%, median, 75%, and 90% $P(O_3)_{net}$, AOC_{VOCs} and the ratio of $P(O_3)_{net}$ to AOC_{VOCs} , respectively.

As expected, the dominant contributor to the AOC during this campaign was OH, followed by O₃ and NO₃. Figure S6-S7 shows the fractional composition of the total AOC. The OH radical contributed about 95.7% of AOC during the daytime (08:00-18:00). O₃, as the second important oxidant, accounted for only 2.9% of AOC during the daytime. The contribution of NO₃ to AOC during the daytime can be ignored, with a contribution of 1.4%. At night, the contributions of O₃ and NO₃ to AOC were higher. OH, O₃ and NO₃ accounted for 75.76%, 6.4%, and 18% in the first half of night (18:00-24:00), and they accounted for 87.87%, 5%, and 7.3% in the second half of night (00:00-08:00).

As the indicator for secondary pollution, net O₃ production rate, $P(O_3)_{net}$, can be calculated from the O₃ formation rate ($F(O_3)$) and the loss rate ($L(O_3)$), as shown in Eq. (5-7) (Tan et al., 2017). The diurnal profiles of the speciation $F(O_3)$ and $L(O_3)$ were shown in Fig. S7-S8 in the Supplementary Information. The diurnal maxima of the modeled $F(O_3)$ and $L(O_3)$ were 18.9 ppb h⁻¹ and 2.8 ppb h⁻¹, with the maximum $P(O_3)_{net}$ of 16.1 ppb h⁻¹ at around 11:00. The modeled $P(O_3)_{net}$ in this study was comparable to the net O₃ production rate in Wangdu site in summer (Tan et al., 2017), while the net ozone production rate in Shenzhen was much higher than the gross O₃ production rate in Beijing in winter it was much higher than the O₃ production rate in Beijing in winter despite being the gross production rate (Tan et al., 2018).

带格式的: 下标

522 $F(O_3) = k_{HO_2+NO}[HO_2][NO] + \sum_i k_{RO_2i+NO} [RO_2]_i[NO]$ (5)

523 $L(O_3) = \theta j(O^1D)[O_3] + k_{O_3+OH}[O_3][OH] + k_{O_3+HO_2}[O_3][HO_2] + (\sum(k_{alkenes+O_3}^i [alkenes^i]))[O_3]$ (6)

524 $P(O_3)_{net} = F(O_3) - L(O_3) - k_{NO_2+OH}[NO_2][OH]$ (7)

525 where θ is the fraction of O^1D from ozone photolysis that reacts with water vapor.

526 Herein, we presented the NO dependence on $P(O_3)_{net}$, AOC_{VOCs} , and the ratio of $P(O_3)_{net}$ to AOC_{VOCs} in Fig. 8 (b-d), in which
 527 AOC_{VOCs} denotes the atmospheric oxidation capacity only from the VOCs oxidation, which includes the channels of primary
 528 VOCs (excluding OVOCs, and mainly alkanes, alkenes, aromatics and isoprene) with OH radicals. An upward trend of $P(O_3)_{net}$
 529 was presented with the increase of NO concentration when NO concentration was below 1 ppb, while $P(O_3)_{net}$ decreased with
 530 the increase of NO concentration because NO_2 became the sink of OH radicals gradually when NO concentration was above
 531 1 ppb. In terms of the NO dependence on AOC_{VOCs} , no significant variation was found, indicating VOCs oxidation was weakly
 532 impacted by NO concentrations in this campaign. Since AOC_{VOCs} can represent the VOCs oxidant rate, and thus the ratio of
 533 $P(O_3)_{net}$ to AOC_{VOCs} can reflect the yield of net ozone production from VOCs oxidation. Similar to $P(O_3)_{net}$, the ratios increased
 534 with the increase of NO concentration when NO concentration was below 1 ppb, while the ratios decreased with the increase
 535 of NO concentration when NO concentration was above 1 ppb, indicating the yield of net O_3 production from VOCs oxidation
 536 would be lower within the low NO regime (< 1 ppb) and high NO regime (> 1 ppb). The median ratios ranged from 1.0 to 4.5,
 537 and the maximum of the median ratios existed when NO concentration was approximately 1 ppb, with a value of approximately
 538 4.5. The nonlinear response of the yield of net ozone production to NO indicated that it is necessary to optimize the NOx and
 539 VOC control strategies for the reduction of O_3 pollution effectively.

540

541 5 Conclusions

542 The STORM field campaign was carried out at Shenzhen site in the autumn of 2018, providing the continuous OH and HO_2^*
 543 observations in PRD since the Heshan campaign in 2014. The maximum diurnal OH and HO_2^* concentrations, which were
 544 measured by PKU-LIF system, were $4.5 \times 10^6 \text{ cm}^{-3}$ and $4.2 \times 10^8 \text{ cm}^{-3}$, respectively. The observed OH concentration was equal
 545 to that measured at Heshan site (autumn campaign) but was lower than those measured in summer campaigns in China
 546 (Backgarden, Yufa, Wangdu, Taizhou and Chengdu sites). The observed HO_2^* concentrations included the true HO_2
 547 concentrations and an estimated interference from RO_2 radicals, and was much lower than those measured at the Backgarden
 548 and Yufa sites in China.

549 The base model (RACM2-LIM1) could reproduce the observed OH concentration before 10:00, and thereafter, OH was
 550 underestimated by the model when NO concentration dropped to low levels. The results of the radical experimental budget
 551 indicated that OH underestimation was likely attributable to an unknown missing OH source at low NO regime. We diagnosed

552 the missing OH source by sensitivity runs, and unclassical OH recycling was identified again in this study. Good agreement
553 between the modeled and observed OH concentrations was achieved when a constant mixing ratio of the numerical species X,
554 equivalent to 0.1 ppb NO, was added into the base model. Additionally, we found isoprene and OVOCs might closely influence
555 the missing OH sources by comparing the composition of VOCs reactivity under the different NO intervals. Isoprene
556 isomerization mechanism (LIM1) can explain approximately 7% of the missing OH production rate, and no significant
557 contribution of MACR and MVK oxidation was found. As another potential OH source, OVOCs species should be further
558 explored to explain the remaining missing OH sources. As for HO₂ radicals, the overestimation of HO₂ concentration was
559 found, indicating that HO₂ heterogeneous uptake with the effective uptake coefficient of 0.3 might make a significant role in
560 HO₂ sinks. Good agreements of OH observations-simulations and HO₂ observations-simulations were both achieved when
561 the amount of X changed from 0.1 ppb to 0.25 ppb and the HO₂ effective uptake coefficient was 0.3.

562 The quantification of production and destruction channels of ROx radicals is essential to explore the chemical processes of
563 radicals. The ROx primary production and termination rates were balanced for the entire day, with maxima of 4 ppb h⁻¹, similar
564 to those at the Heshan and Wangdu sites. Photolysis channels dominated the ROx primary production rate, and the HONO, O₃,
565 HCHO, and carbonyls photolysis accounted for 29%, 16%, 16%, and 11% during the daytime, respectively. The most fraction
566 of ROx termination rate came from the reaction of OH + NO₂ in the morning. The radical self-combination gradually became
567 the major sink of ROx in the afternoon with the decreasing of NO concentrations. The reaction of OH + NO₂ and radical self-
568 combination accounted for 35% and 24% during the daytime, respectively.

569 In this campaign, AOC exhibited well-defined diurnal patterns, with a peak of 11.8 ppb h⁻¹. As expected, OH radicals, which
570 were the dominant oxidant, accounted for 95.7% of the total AOC during the daytime. O₃ and NO₃ contributed 2.9% and 1.4%
571 to total AOC during the daytime, respectively. The ratio of $P(O_3)_{net}$ to AOC_{VOCs} , which denotes the yield of net ozone production
572 from VOCs oxidation, tended to increase and then decrease as NO concentration increased, with a range of 1.0-4.5. Optimizing
573 the NOx and VOCs control strategies might be significant to realize the reduction of ozone concentrations based on the
574 nonlinear relationship between the yield of net ozone production from VOCs oxidation and NO concentrations.

575
576 **Data availability.** The data used in this study are available from the corresponding author upon request (k.lu@pku.edu.cn).

577
578 **Author contributions.** YH Zhang and KD Lu conceived the study. XP Yang analyzed the data and wrote the manuscript with
579 inputs from KD Lu. XP Yang, XF Ma, Y Gao contributed to the measurements of the HOx concentrations. All authors
580 contributed to the discussed results and commented on the manuscript.

581
582 **Competing interests.** The authors declare that they have no conflict of interest.

583

带格式的: 字体: 10 磅

带格式的: 字体: 10 磅

带格式的: 字体: 10 磅

带格式的: 字体: 10 磅

带格式的: 字体: 10 磅

584 **Acknowledgment.** The authors thank the science teams of the STORM-2018 campaign. This work was supported by the
585 Beijing Municipal Natural Science Foundation for Distinguished Young Scholars (JQ19031), the National Research Program
586 for Key Issue in Air Pollution Control (2019YFC0214800), and the National Natural Science Foundation of China (Grants
587 No. 91544225, 21522701, 91844301).

588 Appendix A. Supplementary data

589 References

- 590 Berndt, T., Chen, J., Kjaergaard, E. R., Moller, K. H., Tilgner, A., Hoffmann, E. H., Herrmann, H., Crouse, J. D., Wennberg,
591 P. O., and Kjaergaard, H. G.: Hydrotrioxide (ROOOH) formation in the atmosphere, *Science*, 376, 979-+,
592 10.1126/science.abn6012, 2022.
- 593 Brocco, D., Fratarcangeli, R., Lepore, L., Petricca, M., and Ventrone, I.: Determination of aromatic hydrocarbons in urban air
594 of Rome, *Atmospheric Environment*, 31, 557-566, 10.1016/s1352-2310(96)00226-9, 1997.
- 595 Chen, X., Wang, H., Liu, Y., Su, R., Wang, H., Lou, S., and Lu, K.: Spatial characteristics of the nighttime oxidation capacity
596 in the Yangtze River Delta, China, *Atmospheric Environment*, 208, 150-157, 10.1016/j.atmosenv.2019.04.012, 2019.
- 597 Ehhalt, D. H.: Photooxidation of trace gases in the troposphere, *Physical Chemistry Chemical Physics*, 1, 5401-5408,
598 10.1039/a905097c, 1999.
- 599 Elshorbany, Y. F., Kurtenbach, R., Wiesen, P., Lissi, E., Rubio, M., Villena, G., Gramsch, E., Rickard, A. R., Pilling, M. J., and
600 Kleffmann, J.: Oxidation capacity of the city air of Santiago, Chile, *Atmospheric Chemistry and Physics*, 9, 2257-2273,
601 10.5194/acp-9-2257-2009, 2009.
- 602 Fan, S., Wang, A., Fan, Q., Liu, J., and Wang, B.: ATMOSPHERIC BOUNDARY LAYER CONCEPT MODEL OF THE
603 PEARL RIVER DELTA AND ITS APPLICATION, *Journal of Tropical Meteorology*, 21, 286-292, 2005.
- 604 Feng, T., Zhao, S. Y., Hu, B., Bei, N. F., Zhang, X., Wu, J. R., Li, X., Liu, L., Wang, R. N., Tie, X. X., and Li, G. H.: Assessment
605 of Atmospheric Oxidizing Capacity Over the Beijing-Tianjin-Hebei (BTH) Area, China, *Journal of Geophysical Research-*
606 *Atmospheres*, 126, 18, 10.1029/2020jd033834, 2021.
- 607 Fittschen, C.: The reaction of peroxy radicals with OH radicals, *Chemical Physics Letters*, 725, 102-108,
608 10.1016/j.cplett.2019.04.002, 2019.
- 609 Fittschen, C., Al Ajami, M., Batut, S., Ferracci, V., Archer-Nicholls, S., Archibald, A. T., and Schoemaeker, C.: ROOOH: a
610 missing piece of the puzzle for OH measurements in low-NO environments?, *Atmospheric Chemistry and Physics*, 19, 349-
611 362, 10.5194/acp-19-349-2019, 2019.
- 612 Fuchs, H., Holland, F., and Hofzumahaus, A.: Measurement of tropospheric RO₂ and HO₂ radicals by a laser-induced
613 fluorescence instrument, *Review of Scientific Instruments*, 79, 10.1063/1.2968712, 2008.
- 614 Fuchs, H., Bohn, B., Hofzumahaus, A., Holland, F., Lu, K. D., Nehr, S., Rohrer, F., and Wahner, A.: Detection of HO₂ by laser-
615 induced fluorescence: calibration and interferences from RO₂ radicals, *Atmospheric Measurement Techniques*, 4, 1209-1225,
616 10.5194/amt-4-1209-2011, 2011.
- 617 Fuchs, H., Acir, I. H., Bohn, B., Brauers, T., Dorn, H. P., Häseler, R., Hofzumahaus, A., Holland, F., Kaminski, M., Li, X., Lu,
618 K., Lutz, A., Nehr, S., Rohrer, F., Tillmann, R., Wegener, R., and Wahner, A.: OH regeneration from methacrolein oxidation
619 investigated in the atmosphere simulation chamber SAPHIR, *Atmos. Chem. Phys.*, 14, 7895-7908, 10.5194/acp-14-7895-2014,
620 2014.
- 621 Fuchs, H., Tan, Z., Hofzumahaus, A., Broch, S., Dorn, H.-P., Holland, F., Kuenstler, C., Gomm, S., Rohrer, F., Schrade, S.,
622 Tillmann, R., and Wahner, A.: Investigation of potential interferences in the detection of atmospheric RO_x radicals by laser-
623 induced fluorescence under dark conditions, *Atmospheric Measurement Techniques*, 9, 1431-1447, 10.5194/amt-9-1431-2016,
624 2016.

域代码已更改

带格式的: 字体: (默认) Times New Roman

625 Fuchs, H., Tan, Z., Lu, K., Bohn, B., Broch, S., Brown, S. S., Dong, H., Gomm, S., Haeseler, R., He, L., Hofzumahaus, A.,
626 Holland, F., Li, X., Liu, Y., Lu, S., Min, K.-E., Rohrer, F., Shao, M., Wang, B., Wang, M., Wu, Y., Zeng, L., Zhang, Y., Wahner,
627 A., and Zhang, Y.: OH reactivity at a rural site (Wangdu) in the North China Plain: contributions from OH reactants and
628 experimental OH budget, *Atmospheric Chemistry and Physics*, 17, 645-661, 10.5194/acp-17-645-2017, 2017.

629 Fuchs, H., Albrecht, S., Acir, I.-H., Bohn, B., Breitenlechner, M., Dorn, H.-P., Gkatzelis, G. I., Hofzumahaus, A., Holland, F.,
630 Kaminski, M., Keutsch, F. N., Novelli, A., Reimer, D., Rohrer, F., Tillmann, R., Vereecken, L., Wegener, R., Zaytsev, A.,
631 Kiendler-Scharr, A., and Wahner, A.: Investigation of the oxidation of methyl vinyl ketone (MVK) by OH radicals in the
632 atmospheric simulation chamber SAPHIR, *Atmospheric Chemistry and Physics*, 18, 8001-8016, 10.5194/acp-18-8001-2018,
633 2018.

634 Gao, M., Li, H., Li, Y., Wei, J., Sun, Y., He, L., and Huang, X.: Source characteristics of water-soluble organic matters in
635 PM_{2.5} in the winter of Shenzhen, China *Environmental Science*, 38, 4017-4022, 2018.

636 Geyer, A., Alicke, B., Konrad, S., Schmitz, T., Stutz, J., and Platt, U.: Chemistry and oxidation capacity of the nitrate radical
637 in the continental boundary layer near Berlin, *Journal of Geophysical Research-Atmospheres*, 106, 8013-8025,
638 10.1029/2000jd900681, 2001.

639 Heard, D. E., and Pilling, M. J.: Measurement of OH and HO₂ in the troposphere, *Chemical Reviews*, 103, 5163-5198,
640 10.1021/cr020522s, 2003.

641 Hofzumahaus, A., Aschmutat, U., Hessling, M., Holland, F., and Ehhalt, D. H.: The measurement of tropospheric OH radicals
642 by laser-induced fluorescence spectroscopy during the POPCORN field campaign, *Geophysical Research Letters*, 23, 2541-
643 2544, 10.1029/96gl02205, 1996.

644 Hofzumahaus, A., Rohrer, F., Lu, K., Bohn, B., Brauers, T., Chang, C.-C., Fuchs, H., Holland, F., Kita, K., Kondo, Y., Li, X.,
645 Lou, S., Shao, M., Zeng, L., Wahner, A., and Zhang, Y.: Amplified Trace Gas Removal in the Troposphere, *Science*, 324, 1702-
646 1704, 10.1126/science.1164566, 2009.

647 Holland, F., Hessling, M., and Hofzumahaus, A.: IN-SITU MEASUREMENT OF TROPOSPHERIC OH RADICALS BY
648 LASER-INDUCED FLUORESCENCE - A DESCRIPTION OF THE KFA INSTRUMENT, *Journal of the Atmospheric*
649 *Sciences*, 52, 3393-3401, 10.1175/1520-0469(1995)052<3393:ismoto>2.0.Co;2, 1995.

650 Huang, X.-F., Chen, D.-L., Lan, Z.-J., Feng, N., He, L.-Y., Yu, G.-H., and Luan, S.-J.: Characterization of organic aerosol in
651 fine particles in a mega-city of South China: Molecular composition, seasonal variation, and size distribution, *Atmospheric*
652 *Research*, 114-115, 28-37, <https://doi.org/10.1016/j.atmosres.2012.05.019>, 2012a.

653 Huang, X.-F., Sun, T.-L., Zeng, L.-W., Yu, G.-H., and Luan, S.-J.: Black carbon aerosol characterization in a coastal city in
654 South China using a single particle soot photometer, *Atmospheric Environment*, 51, 21-28,
655 <https://doi.org/10.1016/j.atmosenv.2012.01.056>, 2012b.

656 Jones, C. E., Hopkins, J. R., and Lewis, A. C.: In situ measurements of isoprene and monoterpenes within a south-east Asian
657 tropical rainforest, *Atmospheric Chemistry and Physics*, 11, 6971-6984, 10.5194/acp-11-6971-2011, 2011.

658 Kanaya, Y., Sadanaga, Y., Matsumoto, J., Sharma, U. K., Hirokawa, J., Kajii, Y., and Akimoto, H.: Daytime HO₂ concentrations
659 at Oki Island, Japan, in summer 1998: Comparison between measurement and theory, *Journal of Geophysical Research-*
660 *Atmospheres*, 105, 24205-24222, 10.1029/2000jd900308, 2000.

661 Kanaya, Y., Cao, R., Kato, S., Miyakawa, Y., Kajii, Y., Tanimoto, H., Yokouchi, Y., Mochida, M., Kawamura, K., and Akimoto,
662 H.: Chemistry of OH and HO₂ radicals observed at Rishiri Island, Japan, in September 2003: Missing daytime sink of HO₂
663 and positive nighttime correlations with monoterpenes, *Journal of Geophysical Research-Atmospheres*, 112,
664 10.1029/2006jd007987, 2007.

665 Lelieveld, J., Butler, T. M., Crowley, J. N., Dillon, T. J., Fischer, H., Ganzeveld, L., Harder, H., Lawrence, M. G., Martinez,
666 M., Taraborrelli, D., and Williams, J.: Atmospheric oxidation capacity sustained by a tropical forest, *Nature*, 452, 737-740,
667 10.1038/nature06870, 2008.

668 Levy, H.: NORMAL ATMOSPHERE - LARGE RADICAL AND FORMALDEHYDE CONCENTRATIONS PREDICTED,
669 *Science*, 173, 141-&, 10.1126/science.173.3992.141, 1971.

670 Li, K., Jacob, D. J., Liao, H., Shen, L., Zhang, Q., and Bates, K. H.: Anthropogenic drivers of 2013-2017 trends in summer
671 surface ozone in China, *Proceedings of the National Academy of Sciences of the United States of America*, 116, 422-427,

带格式的: 字体: (默认) Times New Roman

带格式的: 字体: (默认) Times New Roman

带格式的: 字体: (默认) Times New Roman

带格式的: 字体: (默认) Times New Roman

672 10.1073/pnas.1812168116, 2019.

673 Li, Z., Xue, L., Yang, X., Zha, Q., Tham, Y. J., Yan, C., Louie, P. K. K., Luk, C. W. Y., Wang, T., and Wang, W.: Oxidizing
674 capacity of the rural atmosphere in Hong Kong, Southern China, *Science of the Total Environment*, 612, 1114-1122,
675 10.1016/j.scitotenv.2017.08.310, 2018.

676 Liu, S., Li, X., Shen, X., Zeng, L., Huang, X., Zhu, B., Lin, L., and Lou, S.: Measurement and partition analysis of atmospheric
677 OH reactivity in autumn in Shenzhen, *Acta Scientiae Circumstantiae*, 39, 3600-3610, 2019.

678 Liu, Z., Wang, Y., Hu, B., Lu, K., Tang, G., Ji, D., Yang, X., Gao, W., Xie, Y., Liu, J., Yao, D., Yang, Y., and Zhang, Y.:
679 Elucidating the quantitative characterization of atmospheric oxidation capacity in Beijing, China, *Science of the Total*
680 *Environment*, 771, 10.1016/j.scitotenv.2021.145306, 2021.

681 Lou, S., Holland, F., Rohrer, F., Lu, K., Bohn, B., Brauers, T., Chang, C. C., Fuchs, H., Haeseler, R., Kita, K., Kondo, Y., Li,
682 X., Shao, M., Zeng, L., Wahner, A., Zhang, Y., Wang, W., and Hofzumahaus, A.: Atmospheric OH reactivities in the Pearl
683 River Delta - China in summer 2006: measurement and model results, *Atmospheric Chemistry and Physics*, 10, 11243-11260,
684 10.5194/acp-10-11243-2010, 2010.

685 Lu, K., Guo, S., Tan, Z., Wang, H., Shang, D., Liu, Y., Li, X., Wu, Z., Hu, M., and Zhang, Y.: Exploring atmospheric free-
686 radical chemistry in China: the self-cleansing capacity and the formation of secondary air pollution, *National Science Review*,
687 6, 579-594, 10.1093/nsr/nwy073, 2019.

688 Lu, K. D., Rohrer, F., Holland, F., Fuchs, H., Bohn, B., Brauers, T., Chang, C. C., Haeseler, R., Hu, M., Kita, K., Kondo, Y.,
689 Li, X., Lou, S. R., Nehr, S., Shao, M., Zeng, L. M., Wahner, A., Zhang, Y. H., and Hofzumahaus, A.: Observation and modelling
690 of OH and HO₂ concentrations in the Pearl River Delta 2006: a missing OH source in a VOC rich atmosphere, *Atmospheric*
691 *Chemistry and Physics*, 12, 1541-1569, 10.5194/acp-12-1541-2012, 2012.

692 Lu, K. D., Hofzumahaus, A., Holland, F., Bohn, B., Brauers, T., Fuchs, H., Hu, M., Haeseler, R., Kita, K., Kondo, Y., Li, X.,
693 Lou, S. R., Oebel, A., Shao, M., Zeng, L. M., Wahner, A., Zhu, T., Zhang, Y. H., and Rohrer, F.: Missing OH source in a
694 suburban environment near Beijing: observed and modelled OH and HO₂ concentrations in summer 2006, *Atmospheric*
695 *Chemistry and Physics*, 13, 1057-1080, 10.5194/acp-13-1057-2013, 2013.

696 Ma, X., Tan, Z., Lu, K., Yang, X., Liu, Y., Li, S., Li, X., Chen, S., Novelli, A., Cho, C., Zeng, L., Wahner, A., and Zhang, Y.:
697 Winter photochemistry in Beijing: Observation and model simulation of OH and HO₂ radicals at an urban site, *Science of the*
698 *Total Environment*, 685, 85-95, 10.1016/j.scitotenv.2019.05.329, 2019a.

699 Ma, X., Tan, Z., Lu, K., Yang, X., Chen, X., Wang, H., Chen, S., Fang, X., Li, S., Li, X., Liu, J., Liu, Y., Lou, S., Qiu, W.,
700 Wang, H., Zeng, L., and Zhang, Y.: OH and HO₂ radical chemistry at a suburban site during the EXPLORE-YRD campaign
701 in 2018, *Atmospheric Chemistry and Physics*, 22, 7005-7028, 10.5194/acp-22-7005-2022, 2022a.

702 Ma, X. F., Tan, Z. F., Lu, K. D., Yang, X. P., Chen, X. R., Wang, H. C., Chen, S. Y., Fang, X., Li, S. L., Li, X., Liu, J. W., Liu,
703 Y., Lou, S. R., Qiu, W. Y., Wang, H. L., Zeng, L. M., and Zhang, Y. H.: OH and HO₂ radical chemistry at a suburban site during
704 the EXPLORE-YRD campaign in 2018, *Atmospheric Chemistry and Physics*, 22, 7005-7028, 10.5194/acp-22-7005-2022,
705 2022b.

706 Ma, X. Y., Jia, H. L., Sha, T., An, J. L., and Tian, R.: Spatial and seasonal characteristics of particulate matter and gaseous
707 pollution in China: Implications for control policy, *Environmental Pollution*, 248, 421-428, 10.1016/j.envpol.2019.02.038,
708 2019b.

709 Mao, J., Jacob, D. J., Evans, M. J., Olson, J. R., Ren, X., Brune, W. H., St Clair, J. M., Crouse, J. D., Spencer, K. M., Beaver,
710 M. R., Wennberg, P. O., Cubison, M. J., Jimenez, J. L., Fried, A., Weibring, P., Walega, J. G., Hall, S. R., Weinheimer, A. J.,
711 Cohen, R. C., Chen, G., Crawford, J. H., McNaughton, C., Clarke, A. D., Jaegle, L., Fisher, J. A., Yantosca, R. M., Le Sager,
712 P., and Carouge, C.: Chemistry of hydrogen oxide radicals (HOx) in the Arctic troposphere in spring, *Atmospheric Chemistry*
713 *and Physics*, 10, 5823-5838, 10.5194/acp-10-5823-2010, 2010.

714 Mao, J., Ren, X., Zhang, L., Van Duin, D. M., Cohen, R. C., Park, J. H., Goldstein, A. H., Paulot, F., Beaver, M. R., Crouse,
715 J. D., Wennberg, P. O., DiGangi, J. P., Henry, S. B., Keutsch, F. N., Park, C., Schade, G. W., Wolfe, G. M., Thornton, J. A., and
716 Brune, W. H.: Insights into hydroxyl measurements and atmospheric oxidation in a California forest, *Atmospheric Chemistry*
717 *and Physics*, 12, 8009-8020, 10.5194/acp-12-8009-2012, 2012.

718 Novelli, A., Ernst, K., Ernest, C. T., Kubistin, D., Regelin, E., Elste, T., Plass-Duelmer, C., Martinez, M., Lelieveld, J., and

719 Harder, H.: Characterisation of an inlet pre-injector laser-induced fluorescence instrument for the measurement of atmospheric
720 hydroxyl radicals, *Atmospheric Measurement Techniques*, 7, 3413-3430, 10.5194/amt-7-3413-2014, 2014.

721 Peeters, J., Nguyen, T. L., and Vereecken, L.: HOx radical regeneration in the oxidation of isoprene, *Physical Chemistry
722 Chemical Physics*, 11, 5935-5939, 10.1039/b908511d, 2009.

723 Peeters, J., and Muller, J.-F.: HOx radical regeneration in isoprene oxidation via peroxy radical isomerisations. II: experimental
724 evidence and global impact, *Physical Chemistry Chemical Physics*, 12, 14227-14235, 10.1039/c0cp00811g, 2010.

725 Peeters, J., Muller, J.-F., Stavrou, T., and Vinh Son, N.: Hydroxyl Radical Recycling in Isoprene Oxidation Driven by
726 Hydrogen Bonding and Hydrogen Tunneling: The Upgraded LIM1 Mechanism, *Journal of Physical Chemistry A*, 118, 8625-
727 8643, 10.1021/jp5033146, 2014.

728 Ren, X., Olson, J. R., Crawford, J. H., Brune, W. H., Mao, J., Long, R. B., Chen, Z., Chen, G., Avery, M. A., Sachse, G. W.,
729 Barrick, J. D., Diskin, G. S., Huey, L. G., Fried, A., Cohen, R. C., Heikes, B., Wennberg, P. O., Singh, H. B., Blake, D. R., and
730 Shetter, R. E.: HOx chemistry during INTEX-A 2004: Observation, model calculation, and comparison with previous studies,
731 *Journal of Geophysical Research-Atmospheres*, 113, 10.1029/2007jd009166, 2008.

732 Shu, L., Wang, T. J., Han, H., Xie, M., Chen, P. L., Li, M. M., and Wu, H.: Summertime ozone pollution in the Yangtze River
733 Delta of eastern China during 2013-2017: Synoptic impacts and source apportionment, *Environmental Pollution*, 257,
734 10.1016/j.envpol.2019.113631, 2020.

735 Song, H., Zou, Q., and Lu, K.: Parameterization and Application of Hydroperoxyl Radicals (HO₂) Heterogeneous Uptake
736 Coefficient, *Progress in Chemistry*, 33, 1161-1173, 10.7536/pc200749, 2021.

737 Song, H., Lu, K., Dong, H., Tan, Z., Chen, S., Zeng, L., and Zhang, Y.: Reduced Aerosol Uptake of Hydroperoxyl Radical May
738 Increase the Sensitivity of Ozone Production to Volatile Organic Compounds, *Environmental Science & Technology Letters*,
739 9, 22-29, 10.1021/acs.estlett.1c00893, 2022.

740 Stevens, P. S., Mather, J. H., Brune, W. H., Eisele, F., Tanner, D., Jefferson, A., Cantrell, C., Shetter, R., Sewall, S., Fried, A.,
741 Henry, B., Williams, E., Baumann, K., Goldan, P., and Kuster, W.: HO₂/OH and RO₂(2)/HO₂ ratios during the Tropospheric
742 OH Photochemistry Experiment: Measurement and theory, *Journal of Geophysical Research-Atmospheres*, 102, 6379-6391,
743 10.1029/96jd01704, 1997.

744 Stone, D., Whalley, L. K., and Heard, D. E.: Tropospheric OH and HO₂ radicals: field measurements and model comparisons,
745 *Chemical Society Reviews*, 41, 6348-6404, 10.1039/c2cs35140d, 2012.

746 Stone, D., Evans, M. J., Walker, H., Ingham, T., Vaughan, S., Ouyang, B., Kennedy, O. J., McLeod, M. W., Jones, R. L.,
747 Hopkins, J., Punjabi, S., Lidster, R., Hamilton, J. F., Lee, J. D., Lewis, A. C., Carpenter, L. J., Forster, G., Oram, D. E., Reeves,
748 C. E., Bauguitte, S., Morgan, W., Coe, H., Aruffo, E., Dari-Salisburgo, C., Giammaria, F., Di Carlo, P., and Heard, D. E.:
749 Radical chemistry at night: comparisons between observed and modelled HOx, NO₃ and N₂O₅ during the RONOCO project,
750 *Atmospheric Chemistry and Physics*, 14, 1299-1321, 10.5194/acp-14-1299-2014, 2014.

751 Taketani, F., Kanaya, Y., Pochanart, P., Liu, Y., Li, J., Okuzawa, K., Kawamura, K., Wang, Z., and Akimoto, H.: Measurement
752 of overall uptake coefficients for HO₂ radicals by aerosol particles sampled from ambient air at Mts. Tai and Mang (China),
753 *Atmospheric Chemistry and Physics*, 12, 11907-11916, 10.5194/acp-12-11907-2012, 2012.

754 Tan, Z., Fuchs, H., Lu, K., Hofzumahaus, A., Bohn, B., Broch, S., Dong, H., Gomm, S., Haeseler, R., He, L., Holland, F., Li,
755 X., Liu, Y., Lu, S., Rohrer, F., Shao, M., Wang, B., Wang, M., Wu, Y., Zeng, L., Zhang, Y., Wahner, A., and Zhang, Y.: Radical
756 chemistry at a rural site (Wangdu) in the North China Plain: observation and model calculations of OH, HO₂ and RO₂ radicals,
757 *Atmospheric Chemistry and Physics*, 17, 663-690, 10.5194/acp-17-663-2017, 2017.

758 Tan, Z., Rohrer, F., Lu, K., Ma, X., Bohn, B., Broch, S., Dong, H., Fuchs, H., Gkatzelis, G. I., Hofzumahaus, A., Holland, F.,
759 Li, X., Liu, Y., Liu, Y., Novelli, A., Shao, M., Wang, H., Wu, Y., Zeng, L., Hu, M., Kiendler-Scharr, A., Wahner, A., and Zhang,
760 Y.: Wintertime photochemistry in Beijing: observations of ROx radical concentrations in the North China Plain during the
761 BEST-ONE campaign, *Atmospheric Chemistry and Physics*, 18, 12391-12411, 10.5194/acp-18-12391-2018, 2018.

762 Tan, Z., Lu, K., Hofzumahaus, A., Fuchs, H., Bohn, B., Holland, F., Liu, Y., Rohrer, F., Shao, M., Sun, K., Wu, Y., Zeng, L.,
763 Zhang, Y., Zou, Q., Kiendler-Scharr, A., Wahner, A., and Zhang, Y.: Experimental budgets of OH, HO₂, and RO₂ radicals and
764 implications for ozone formation in the Pearl River Delta in China 2014, *Atmospheric Chemistry and Physics*, 19, 7129-7150,
765 10.5194/acp-19-7129-2019, 2019.

766 Tan, Z., Hofzumahaus, A., Lu, K., Brown, S. S., Holland, F., Huey, L. G., Kiendler-Scharr, A., Li, X., Liu, X., Ma, N., Min,
767 K.-E., Rohrer, F., Shao, M., Wahner, A., Wang, Y., Wiedensohler, A., Wu, Y., Wu, Z., Zeng, L., Zhang, Y., and Fuchs, H.: No
768 Evidence for a Significant Impact of Heterogeneous Chemistry on Radical Concentrations in the North China Plain in Summer
769 2014, *Environmental Science & Technology*, 54, 5973-5979, 10.1021/acs.est.0c00525, 2020.

770 Tan, Z., Ma, X., Lu, K., Jiang, M., Zou, Q., Wang, H., Zeng, L., and Zhang, Y.: Direct evidence of local photochemical
771 production driven ozone episode in Beijing: A case study, *Science of the Total Environment*, 800,
772 10.1016/j.scitotenv.2021.148868, 2021.

773 Wang, T., Xue, L. K., Brimblecombe, P., Lam, Y. F., Li, L., and Zhang, L.: Ozone pollution in China: A review of concentrations,
774 meteorological influences, chemical precursors, and effects, *Science of the Total Environment*, 575, 1582-1596,
775 10.1016/j.scitotenv.2016.10.081, 2017a.

776 Wang, W., Parrish, D. D., Li, X., Shao, M., Liu, Y., Mo, Z., Lu, S., Hu, M., Fang, X., Wu, Y., Zeng, L., and Zhang, Y.: Exploring
777 the drivers of the increased ozone production in Beijing in summertime during 2005-2016, *Atmospheric Chemistry and Physics*,
778 20, 15617-15633, 10.5194/acp-20-15617-2020, 2020.

779 Wang, X., Wang, H., Xue, L., Wang, T., Wang, L., Gu, R., Wang, W., Tham, Y. J., Wang, Z., Yang, L., Chen, J., and Wang, W.:
780 Observations of N2O5 and ClNO2 at a polluted urban surface site in North China: High N2O5 uptake coefficients and low
781 ClNO2 product yields, *Atmospheric Environment*, 156, 125-134, 10.1016/j.atmosenv.2017.02.035, 2017b.

782 Whalley, L. K., Edwards, P. M., Furneaux, K. L., Goddard, A., Ingham, T., Evans, M. J., Stone, D., Hopkins, J. R., Jones, C.
783 E., Karunaharan, A., Lee, J. D., Lewis, A. C., Monks, P. S., Moller, S. J., and Heard, D. E.: Quantifying the magnitude of a
784 missing hydroxyl radical source in a tropical rainforest, *Atmospheric Chemistry and Physics*, 11, 7223-7233, 10.5194/acp-11-
785 7223-2011, 2011.

786 Whalley, L. K., Stone, D., George, I. J., Mertes, S., van Pinxteren, D., Tilgner, A., Herrmann, H., Evans, M. J., and Heard, D.
787 E.: The influence of clouds on radical concentrations: observations and modelling studies of HOx during the Hill Cap Cloud
788 Thuringia (HCCT) campaign in 2010, *Atmospheric Chemistry and Physics*, 15, 3289-3301, 10.5194/acp-15-3289-2015, 2015.

789 Whalley, L. K., Slater, E. J., Woodward-Massey, R., Ye, C., Lee, J. D., Squires, F., Hopkins, J. R., Dunmore, R. E., Shaw, M.,
790 Hamilton, J. F., Lewis, A. C., Mehra, A., Worrall, S. D., Bacak, A., Bannan, T. J., Coe, H., Percival, C. J., Ouyang, B., Jones,
791 R. L., Crilley, L. R., Kramer, L. J., Bloss, W. J., Vu, T., Kotthaus, S., Grimmond, S., Sun, Y., Xu, W., Yue, S., Ren, L., Acton,
792 W. J. F., Hewitt, C. N., Wang, X., Fu, P., and Heard, D. E.: Evaluating the sensitivity of radical chemistry and ozone formation
793 to ambient VOCs and NOx in Beijing, *Atmospheric Chemistry and Physics*, 21, 2125-2147, 10.5194/acp-21-2125-2021, 2021.

794 Xue, L., Gu, R., Wang, T., Wang, X., Saunders, S., Blake, D., Louie, P. K. K., Luk, C. W. Y., Simpson, I., Xu, Z., Wang, Z.,
795 Gao, Y., Lee, S., Mellouki, A., and Wang, W.: Oxidative capacity and radical chemistry in the polluted atmosphere of Hong
796 Kong and Pearl River Delta region: analysis of a severe photochemical smog episode, *Atmospheric Chemistry and Physics*,
797 16, 9891-9903, 10.5194/acp-16-9891-2016, 2016.

798 Yang, X., Wang, H., Tan, Z., Lu, K., and Zhang, Y.: Observations of OH Radical Reactivity in Field Studies, *Acta Chimica*
799 *Sinica*, 77, 613-624, 10.6023/a19030094, 2019.

800 Yang, X., Lu, K., Ma, X., Liu, Y., Wang, H., Hu, R., Li, X., Lou, S., Chen, S., Dong, H., Wang, F., Wang, Y., Zhang, G., Li, S.,
801 Yang, S., Yang, Y., Kuang, C., Tan, Z., Chen, X., Qiu, P., Zeng, L., Xie, P., and Zhang, Y.: Observations and modeling of OH
802 and HO2 radicals in Chengdu, China in summer 2019, *The Science of the total environment*, 772, 144829-144829,
803 10.1016/j.scitotenv.2020.144829, 2021.

804 Yang, Y., Wang, Y., Yao, D., Zhao, S., Yang, S., Ji, D., Sun, J., Wang, Y., Liu, Z., Hu, B., Zhang, R., and Wang, Y.: Significant
805 decreases in the volatile organic compound concentration, atmospheric oxidation capacity and photochemical reactivity during
806 the National Day holiday over a suburban site in the North China Plain, *Environmental Pollution*, 263,
807 10.1016/j.envpol.2020.114657, 2020a.

808 Yang, Y., Wang, Y., Yao, D., Zhao, S., Yang, S., Ji, D., Sun, J., Wang, Y., Liu, Z., Hu, B., Zhang, R., and Wang, Y.: Significant
809 decreases in the volatile organic compound concentration, atmospheric oxidation capacity and photochemical reactivity during
810 the National Day holiday over a suburban site in the North China Plain, *Environmental Pollution*, 263, 114657,
811 <https://doi.org/10.1016/j.envpol.2020.114657>, 2020b.

812 Yu, D., Tan, Z., Lu, K., Ma, X., Li, X., Chen, S., Zhu, B., Lin, L., Li, Y., Qiu, P., Yang, X., Liu, Y., Wang, H., He, L., Huang,

带格式的: 字体: (默认) Times New Roman

带格式的: 字体: (默认) Times New Roman

813 X., and Zhang, Y.: An explicit study of local ozone budget and NO_x-VOCs sensitivity in Shenzhen China, Atmospheric
814 Environment, 224, 117304, <https://doi.org/10.1016/j.atmosenv.2020.117304>, 2020.
815 Zhang, Y. H., Hu, M., Zhong, L. J., Wiedensohler, A., Liu, S. C., Andreae, M. O., Wang, W., and Fan, S. J.: Regional Integrated
816 Experiments on Air Quality over Pearl River Delta 2004 (PRIDE-PRD2004): Overview, Atmospheric Environment, 42, 6157-
817 6173, 10.1016/j.atmosenv.2008.03.025, 2008.
818 Zhou, J., Murano, K., Kohno, N., Sakamoto, Y., and Kajii, Y.: Real-time quantification of the total HO₂ reactivity of ambient
819 air and HO₂ uptake kinetics onto ambient aerosols in Kyoto (Japan), Atmospheric Environment, 223,
820 10.1016/j.atmosenv.2020.117189, 2020.
821 Zhou, J., Sato, K., Bai, Y., Fukusaki, Y., Kousa, Y., Ramasamy, S., Takami, A., Yoshino, A., Nakayama, T., Sadanaga, Y.,
822 Nakashima, Y., Li, J., Murano, K., Kohno, N., Sakamoto, Y., and Kajii, Y.: Kinetics and impacting factors of HO₂ uptake onto
823 submicron atmospheric aerosols during the 2019 Air QUALity Study (AQUAS) in Yokohama, Japan, Atmospheric Chemistry
824 and Physics, 21, 12243-12260, 10.5194/acp-21-12243-2021, 2021.
825 Zhu, J., Wang, S., Wang, H., Jing, S., Lou, S., Saiz-Lopez, A., and Zhou, B.: Observationally constrained modeling of
826 atmospheric oxidation capacity and photochemical reactivity in Shanghai, China, Atmospheric Chemistry and Physics, 20,
827 1217-1232, 10.5194/acp-20-1217-2020, 2020.

带格式的: 字体: (默认) Times New Roman

带格式的: 字体: (默认) Times New Roman

828

域代码已更改